Enyang Lian, Yingyu Ren*, Yunfeng Han, Weixin Liu, Ningde Jin and Junying Zhao

Multi-Scale Morphological Analysis of Conductance Signals in Vertical Upward Gas–Liquid Two-Phase Flow

DOI 10.1515/zna-2016-0235
Received June 13, 2016; accepted September 11, 2016; previously published online October 14, 2016

Abstract: The multi-scale analysis is an important method for detecting nonlinear systems. In this study, we carry out experiments and measure the fluctuation signals from a rotating electric field conductance sensor with eight electrodes. We first use a recurrence plot to recognise flow patterns in vertical upward gas–liquid two-phase pipe flow from measured signals. Then we apply a multi-scale morphological analysis based on the first-order difference scatter plot to investigate the signals captured from the vertical upward gas–liquid two-phase flow loop test. We find that the invariant scaling exponent extracted from the multi-scale first-order difference scatter plot with the bisector of the second-fourth quadrant as the reference line is sensitive to the inhomogeneous distribution characteristics of the flow structure, and the variation trend of the exponent is helpful to understand the process of breakup and coalescence of the gas phase. In addition, we explore the dynamic mechanism influencing the inhomogeneous distribution of the gas phase in terms of adaptive optimal kernel time–frequency representation. The research indicates that the system energy is a factor influencing the distribution of the gas phase and the multi-scale morphological analysis based on the first-order difference scatter plot is an effective method for indicating the inhomogeneous distribution of the gas phase in gas–liquid two-phase flow.

Keywords: Conductance Sensor; Gas–Liquid Two-Phase Flow; Inhomogeneous Distribution; Multi-Scale Morphological Analysis.

***Corresponding author: Yingyu Ren,** School of Electrical Engineering and Automation, Tianjin University, Tianjin 300072, China, E-mail: renyingyuee@tju.edu.cn
Enyang Lian, Yunfeng Han, Weixin Liu and Ningde Jin: School of Electrical Engineering and Automation, Tianjin University, Tianjin 300072, China
Junying Zhao: Electronic Technology Department, Tianjin Vocational College of Electronics and Information Technology, Tianjin 300350, China

1 Introduction

Gas–liquid two-phase flow widely exists in lots of industry production processes such as petroleum industry, chemical engineering, nuclear and thermal engineering, and so on. The flow structure of gas–liquid two-phase flow significantly affects the accuracy of the flow parameter detection. Thus, investigating the dynamic mechanisms of flow structure transformation in gas–liquid two-phase flow makes a lot of sense for understanding the characteristics of the industry process, optimising the sensor design, and improving the flow rate measurement accuracy of gas–liquid two-phase flow.

A large number of scholars have been dedicated to exploring the flow behaviours of gas–liquid two-phase flow [1–3]. As the flow structures encountered in gas–liquid two-phase flow are of extreme complexity arising from the complicated phase interface interaction, it is very difficult to find out the mechanisms of flow pattern transformation. The traditional approaches on flow pattern identification can be classified into direct method and indirect method. The direct method mainly includes the visual method, high-speed camera method, ray attenuation method, and contact probe method. Wallis [4] pointed out that due to complicated reflection phenomena occurred in the complex phase interface, there would be large visual measurement errors while shooting pictures inside fluid even using a high-speed camera. In addition, Barnea et al. [5] utilised multi-probes to detect the changes of flow patterns.

In recent years, flow identification based on the experimental observation data has further developed. According to the power spectrum density distribution of the wall static pressure fluctuation, Hubbard and Dukler [6] analysed the horizontal gas–liquid two-phase flow and defined three kinds of flow patterns, namely, separated flow, dispersed flow, and intermittent flow. Jones and Zuber [7] identified the flow pattern of gas–liquid two-phase flow and obtained bubbly flow, slug flow, and annular flow based on the probability density of local void fraction, measured by using

X-ray. Vince and Lahey [8] employed transient X-ray attenuation techniques and stated the same conclusion as that of Jones and Zuber. Furthermore, big progress was made in identifying flow patterns based on the differential pressure signal of two-phase flow in the pipe [9–11]. Thereafter, many other methods, including wavelet analysis [12–14], Hilbert–Huang transform [15], Wigner–Ville distribution [16–18], recurrence plot [19, 20], complex network [21], and so on were widely used in the analysis of signals obtained from gas–liquid two-phase flow. Besides, the scholars predicted the flow pattern transitional boundaries on the basis of the gas–liquid two-phase flow mechanisms [22–24], which, however, are prone to be influenced by the criteria for the flow pattern conversion.

So far the research studies on gas–liquid two-phase flow are almost restricted to flow parameter measurement and flow pattern identification, and there is still a lack of research on the dispersed bubble size and its distribution in the continuous water phase. As for this problem, the feature invariant (fractal dimension, correlation dimension, K entropy, and complex entropy) extracted by the nonlinear time series analysis method can be a sensitive characteristic, which is able to indicate the change of the fluid structure distribution of gas–liquid two-phase flow [25–27]. Moreover, the nonlinear analysis method has been widely used in investigating different kinds of physiological signals in recent years [28–33], especially the method of multi-scale distribution entropy analysis [34] combined with differential sequence analysis, which can contribute to understanding the dynamics characteristics of heart rate at time scale.

Our research group combined chaotic attractor morphological analysis [35–38] and differential sequence analysis, and further applied it to uncover the inhomogeneous distribution of the dispersed droplets in oil–water flows [39]. Hence, we analysed the signals measured from the vertical gas–liquid two-phase experiment using a rotating electric field conductance sensor with eight electrodes. Then the scaling invariant representing the second-order moment in the first-order difference scatter plot was calculated, and the results show that the scaling invariant is an effective indicator for exposing the inhomogeneous distribution of the dispersed phase, comprehending the dynamics phenomena of coalescence and breakup of the gas phase, and exploring the fluid structure of the gas–liquid two-phase flow.

2 Multi-Scale Morphological Analysis Based on a First-Order Difference Scatter Plot

2.1 Multi-Scale First-Order Difference Scatter Plot

The basic principle of a multi-scale first-order difference scatter plot is as follows: first, obtain coarse-grained time series from the original one, and then construct first-order difference sequences at each scale, and finally present the first-order difference scatter plot. The specific algorithm is given as follows [40].

For a given one-dimensional time series $\{x(i):i=1, 2, \ldots, N\}$, the coarse-grained time series $\{y_j^s:j=1, 2, \ldots, N/s\}$ possesses the form

$$y_j^s=\frac{1}{s}\sum_{i=(j-1)s+1}^{js} x(i),\quad 1\le j\le N/s \tag{1}$$

where s is the scale factor. In particular, the coarse-grained time series is the original one when $s=1$. The length of each coarse-grained time series is equal to the ratio of the length of the original time series to the scale factor s.

Then calculate the difference sequence at each scale:

$$d_i^s=y_{j+1}^s-y_j^s\quad (1\le i\le j-1<N/s-1) \tag{2}$$

Finally, we can plot the scatter points after the first return of the difference sequence d_i^s in the two-dimensional plane, that is, (d_i^s, d_{i+1}^s).

2.2 Reference Section System and Attractor Moment

In order to readily investigate the system movement laws in an N-dimensional space, we construct N orthogonal $(N-1)$-dimensional reference sections referred to as the N-orthogonal reference system.

For arbitrary N-dimensional phase space, we can obtain N-orthogonal unit vectors through the coordinate origin, which can be expressed as

$$\begin{cases}\alpha_1=(a_{11}, a_{12}, \ldots, a_{1N})^{\mathrm{T}}\\ \alpha_2=(a_{21}, a_{22}, \ldots, a_{2N})^{\mathrm{T}}\\ \quad\vdots\\ \alpha_N=(a_{N1}, a_{N2}, \ldots, a_{NN})^{\mathrm{T}}\end{cases} \tag{3}$$

where α_i ($i=1, 2, \ldots, N$) denotes the N vectors, and they are constrained by the following equations:

$$\langle \alpha_i, \alpha_j \rangle = \begin{cases} ||\alpha_i||^2 = 1 & (i=j) \\ 0 & (i \neq j) \end{cases} \tag{4}$$

where $\langle \bullet, \bullet \rangle$ and $\|\bullet, \bullet\|$ are the inner product and the 2-norm in Euclidean space, respectively.

Then take α_i ($i=1, 2, \ldots, N$) as normal vectors to determine the N orthogonal reference sections through the coordinate origin:

$$\begin{cases} a_{11}x_1 + a_{12}x_2 + \cdots + a_{1N}x_N = 0 \\ a_{21}x_1 + a_{22}x_2 + \cdots + a_{2N}x_N = 0 \\ \vdots \\ a_{N1}x_1 + a_{N2}x_2 + \cdots + a_{NN}x_N = 0 \end{cases} \tag{5}$$

Simplify (5) as $X=(x_1, x_2, \ldots, x_N)^T$ and acquire the expression

$$(\alpha_1, \alpha_2, \ldots, \alpha_N)^T X = 0 \tag{6}$$

For the two-dimensional plane, we constructed the reference sections degenerate into two orthogonal lines, one of which is shown in Figure 1 with the normal vector $\alpha_1=(a_{11}, a_{12})^T$. The other one is the line $a_{21}x_1+a_{22}x_2=0$, which is orthogonal with the line illustrated in Figure 1 at the coordinate origin.

In order to quantitatively describe the morphological characteristics of the first-order difference scatter plot, it is necessary to introduce the definition of distance, that is, the distance from each scatter point to the reference line, which can be expressed as

$$d_i(k) = \langle \alpha_i, X(k) \rangle = a_{i1}x_1(k) + a_{i2}x_2(k) \tag{7}$$

where $X(k)=(x_1(k), x_2(k))$ is the coordinate of the kth scatter point and $k=1, 2, \ldots, M$, M is the total number of scatter points. On the basis of the distance defined in (7), we further define the morphological parameter, that is, attractor moment, for a specific time scale s as

$$M_{i,j}(s) = \frac{\sum_{k=1}^{M} d_i(k)^j}{M} \tag{8}$$

where $M_{i,j}(s)$ is the j-order moment of all scatter points to the i-reference line. The even-order attractor moment indicates the dispersion degree of the scatter points to the investigated reference line, while the odd-order attractor moment corresponds to the symmetry of the scatter points to the investigated reference line.

Considering our research objects in this paper, choosing the optimal reference line is of great importance and the key to ensure the correctness of the result. Xiao and Jin [37] concluded that the bisectors of the first-third quadrant and second-fourth quadrant are the two appreciate reference lines in the two-dimensional space which can be used to investigate the two-dimensional attractors of gas–liquid two-phase flow. In terms of our further exploration, we find that it is more appropriate to choose the second-order moment $M_{1,2}(s)$ with the bisector of the second-fourth quadrant being the reference line.

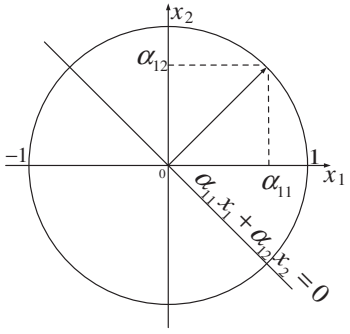

Figure 1: A normal vector and the corresponding reference section (line) in the two-dimensional space.

3 Experimental Facility and Data Acquisition

3.1 Rotating Electric Field Conductance Sensor with Eight Electrodes

Figure 2a shows the structure of the rotating electric field conductance sensor with eight electrodes and its sectional view. The sensor consists of four pairs of half-ring stainless steel electrodes flush-mounted on the inside wall of an insulating pipe, whose structure parameters mainly include opening angle, radial thickness, and axial height, which are set to 22.5°, 1 mm, and 4 mm, respectively, with the aid of geometry optimization by ANSYS. Four pairs of electrodes are excited by four sinusoidal signals with the same electric field intensity, but different phase positions, each of them has a lag of 45°. The compound field intensities are the same but its angle changes with time which can be described by $\phi = wt$. Figure 2b presents the schematic diagram of the rotating field and provides the excited method of the rotating field. Each electrode is at a different initial phase, and the variance of electric potential is in accordance with the sinusoidal signal. Thus, the ultimate electric field in the pipe is synthesised by the four electric

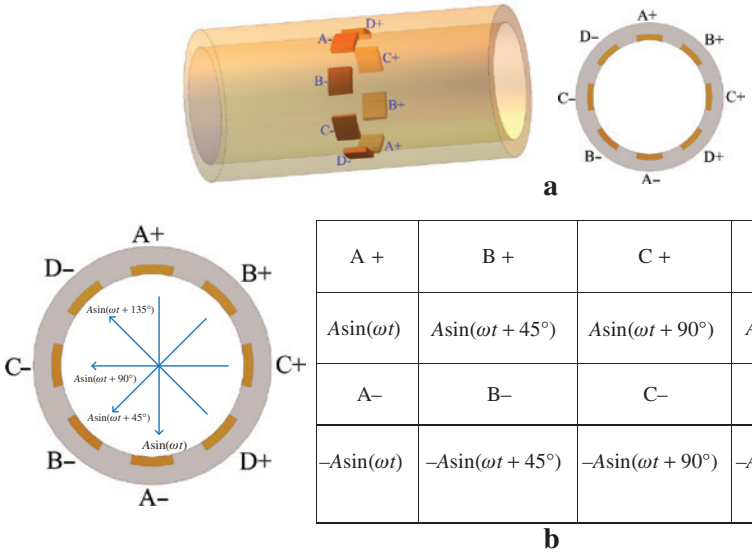

a

A +	B +	C +	D +
$A\sin(\omega t)$	$A\sin(\omega t + 45°)$	$A\sin(\omega t + 90°)$	$A\sin(\omega t + 135°)$
A–	B–	C–	D–
$-A\sin(\omega t)$	$-A\sin(\omega t + 45°)$	$-A\sin(\omega t + 90°)$	$-A\sin(\omega t + 135°)$

b

Figure 2: The rotating electric field conductance sensor with eight electrodes. (a) Three-dimensional structure schematic of the conductance sensor and its sectional view; (b) excitation method of the sensor.

fields possessing different directions, and its direction changes with time to form a rotating electric field.

3.2 Experimental Facility

The vertical upward gas–liquid two-phase flow experiment is carried out in a multiphase flow loop facility and sensor system in Tianjin University. The schematic diagram of the experimental facility is delineated in Figure 3. The testing pipe is a 2310-mm organic glass tube with an inner diameter of 20 mm. The rotating electric field conductance sensor is installed at over 1400 mm height from the inlet. The fluid mediums are tap water and air. At normal atmospheric temperature, the density of water and air is 1000 and 1.29 kg/m^3, respectively. The surface tension between air and water is 0.075 N/m. The transportation and metering of the liquid phase are implemented by means of a peristaltic pump. The gas phase is generated and metered by an air compressor and a rotameter, respectively. Considering the error in the experiment, we adopt the concept of the combined standard uncertainty

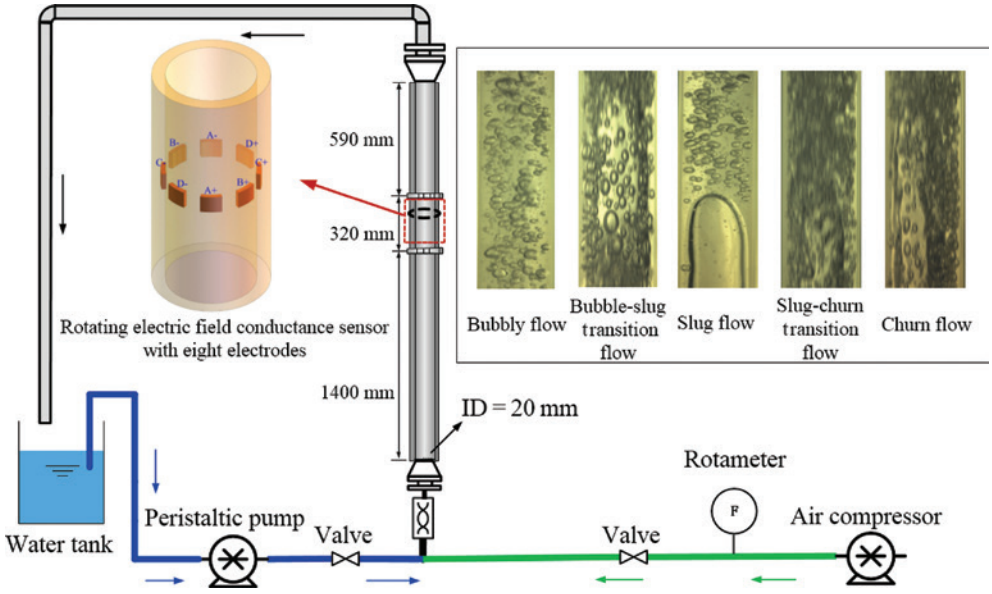

Figure 3: Schematic diagram of the experimental facility.

for error analysis. The accuracy of the peristaltic pump and the rotameter is 1.5 % and 0.2 %, respectively; thus the combined standard uncertainty of the experiment is

$$u_c = \sqrt{(1.5\,\%)^2 + (0.2\,\%)^2} = 1.51\,\%$$

In this experiment, we fix the gas superficial velocity (U_{sg}) at 0.055, 0.074, 0.111, 0.147, 0.221, 0.295, 0.368, 0.479, and 0.589 (m/s) in turn, and then set the liquid superficial velocity (U_{sw}) to 0.037, 0.074, 0.147, 0.295, 0.442, 0.589, 0.737, 0.884, and 1.032 (m/s) at each gas superficial velocity to obtain different flow conditions.

The measurement circuit and data acquisition system of the rotating electric field conductance sensor with eight electrodes is shown in Figure 4. The excitation part adopts a direct digital frequency synthesiser chip AD9959, whose frequency control register and phase control register are controlled by a single-chip STC89LV51 to generate four sinusoidal signals with 10 V amplitude, 20 kHz frequency, and different phase positions, each of them has a lag of 45°. Take A-channel for example; first configure AD9959 to obtain the sinusoidal signal, and then amplify and reverse the signal to generate $5\sin(\omega t)$ V and $-5\sin(\omega t)$ V ($\omega = 2\pi f = 40000\pi$), which are applied to the A+ electrode and the A– electrode, respectively. The current magnitude of the A+ and A– electrodes is then measured by the voltage of reference resistance R_{ref} to reflect the electrical conductivity of fluid in the pipe. Besides, the voltage effective value of R_{ref} is collected through a true root mean square measurement chip AD637. It is similar for B-channel, C-channel, and D-channel, except for the lag of 45°. The data acquisition device, namely, the PXI 4472 data acquisition card (NI Company, Austin, TX, USA), with the combination of graphical programming language LabVIEW 7.1 is utilised to achieve the display of waveform variations, real-time data acquisition, and on-line data calculating and analysis. The sampling frequency is 2000 Hz, and the signals are recorded for 30 s.

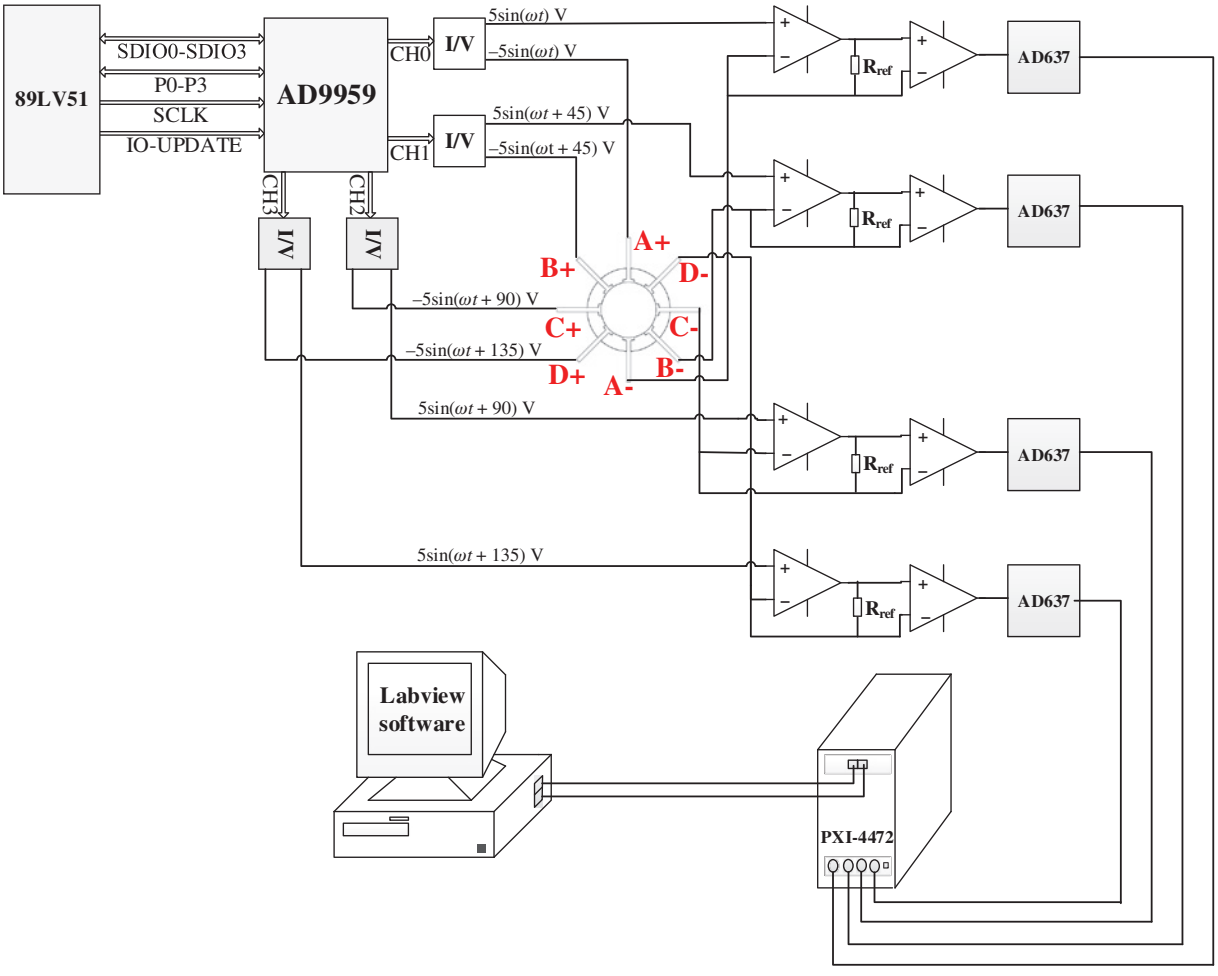

Figure 4: The measurement circuit and data acquisition system of the rotating electric field conductance sensor with eight electrodes.

According to the above settings, we can obtain the conductance fluctuating voltage signals under five kinds of flow patterns, that is, bubbly flow, slug–bubble transition flow, slug flow, slug–churn transition flow, and churn flow.

3.3 Signal Acquisition and Signal Processing

For characterising each component of two-phase flow more effectively, we define that the normalised conductance of gas–liquid two-phase flow G_e equals the ratio of gas–liquid mixture conductance δ_m to pure water conductance δ_w:

$$G_e = \frac{\delta_m}{\delta_w} = \frac{V_m}{V_m^w} \tag{9}$$

where V_m and V_m^w are the mixture measurement voltage for each channel and the mean pure water measurement voltage for the corresponding channel, respectively. On the basis of the normalised conductance sequence, we define the first-order difference conductance ΔG_e as follows:

$$\Delta G_e = G_e(i+1) - G_e(i) \tag{10}$$

The normalised conductance signals and corresponding first-order difference sequences of typical measurement signals from A-channel are shown in Figure 5a and b, respectively.

According to the measurement principle of the conductance sensor, the changes in the amplitude of conductance senor signals can indicate the size variation of the bubble flowing through the measuring area. More specifically, the amplitude of the conductance sensor signal for a large bubble is low, that is, V_m is small, due to which the amplitude of normalised conductance is small. In contrast, the amplitude of the conductance sensor signal for a small bubble is high and the amplitude of normalised conductance is large. When the amplitude of normalised conductance is relatively stable, that is, the bubble size and bubble size distribution in the pipe are relatively homogeneous, the amplitude of the first-order difference sequence will fluctuate slightly near zero. However, when the amplitude of normalised conductance fluctuates heavily, that is, the distribution of the gas phase in the pipe is more inhomogeneous, the amplitude of the first-order difference sequence will fluctuate obviously. Moreover, the fluctuation range increasingly tends to be larger as the distribution of the gas phase becomes more inhomogeneous.

As presented in Figure 5, the amplitude of normalised conductance possesses the smallest fluctuation for the signal of bubbly flow, which reflects the most uniform bubble size distribution and relatively stable fluid

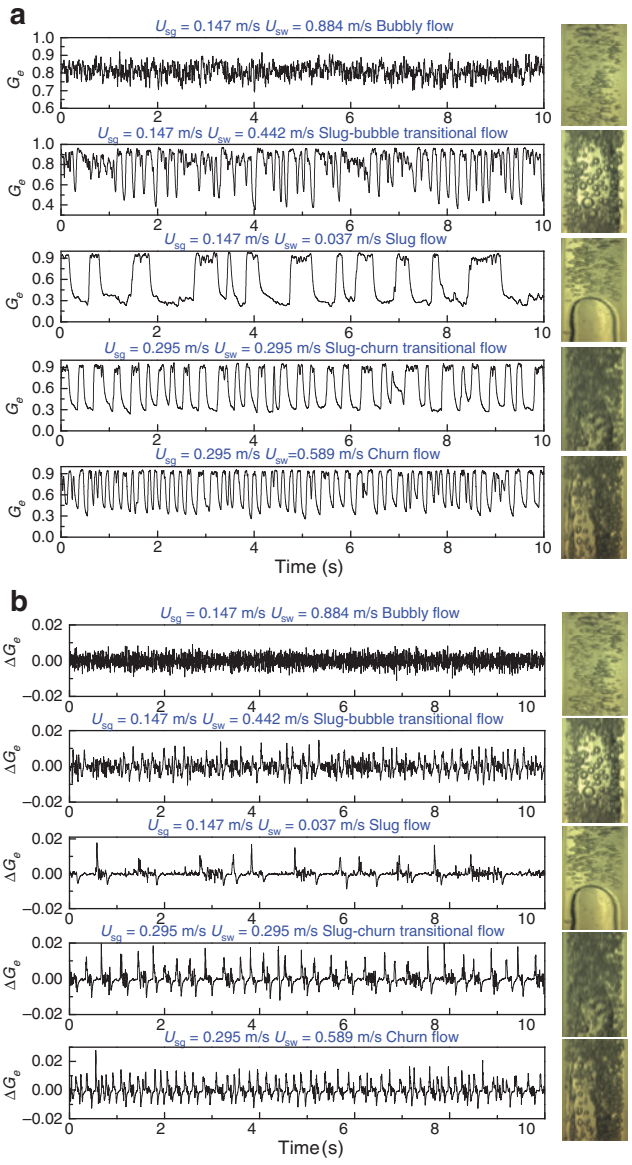

Figure 5: Five typical measurement signals from A-channel: (a) normalised conductance sequences; (b) first-order difference sequences of corresponding normalised conductance sequences.

structure. Besides, the first-order difference sequence basically remains around zero. With a few of slightly large bubbles flowing past occasionally, it will result in a little larger amplitude fluctuation. As to slug–bubble transition flow, a few bubbles coalesce to form short gas slugs, but there are still a lot of bubbles existing between liquid slugs; thus the amplitude of the difference sequence becomes larger and the frequency is lower, which represents a more non-uniform distribution of the gas phase. Along with the coalescence of the bubble to the slug, the flow pattern turns into slug flow. The amplitude of the normalised conductance signal now changes sharply

when the interface flows through the measuring area, but remains almost constant when gas slugs or liquid slugs flow past. Besides, the fluctuation range of the corresponding first-order difference sequence is more severe, which demonstrates the extremely non-uniform distribution of the gas phase. With regard to slug–churn transition flow, some gas slugs are broken up to gas blocks. Thus the fluctuation frequency of the normalised conductance signal increases, and the duration of the amplitude of the first-order difference sequence remaining around zero lasts rather shorter than that of slug flow with a further increase of the fluctuation range. Churn flow appears as water superficial velocity increases. The gas phase exists as gas blocks scattering in the continuous water phase; thus the difference sequence keeps fluctuating. Compared with slug–churn transition flow, the churn flow is more

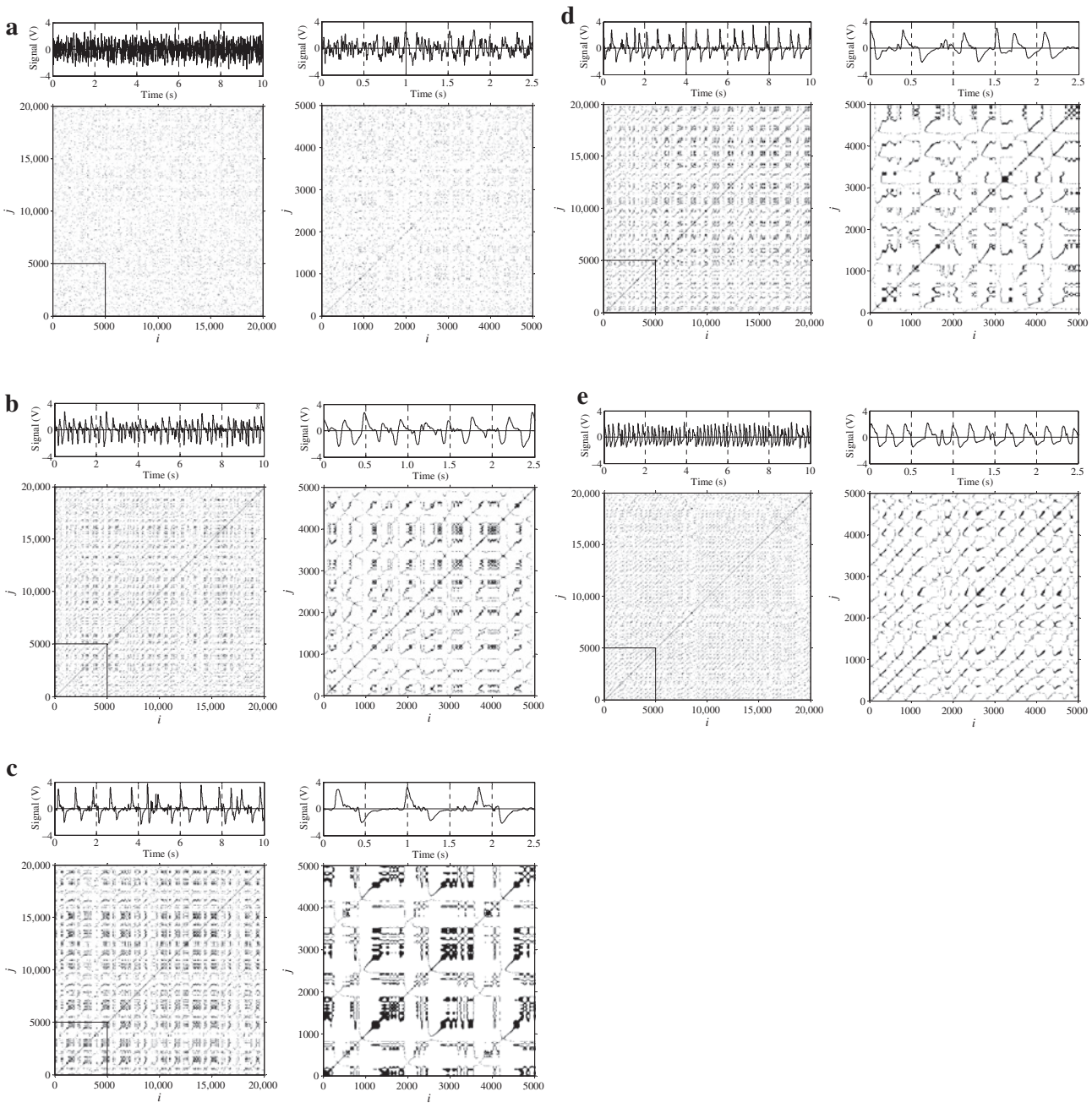

Figure 6: Recurrence plot of five typical flow patterns: (a) bubbly flow ($U_{sg} = 0.147$ m/s, $U_{sw} = 0.884$ m/s); (b) slug–bubble transitional flow ($U_{sg} = 0.147$ m/s, $U_{sw} = 0.442$ m/s); (c) slug flow ($U_{sg} = 0.147$ m/s, $U_{sw} = 0.037$ m/s); (d) slug–churn transitional flow ($U_{sg} = 0.295$ m/s, $U_{sw} = 0.295$ m/s); (e) churn flow ($U_{sg} = 0.295$ m/s, $U_{sw} = 0.589$ m/s).

uniform, which reflects a smaller fluctuation range of the first-order difference sequence.

3.4 Identification of Gas–Liquid Two-Phase Flow Patterns

Recurrence plot is a nonlinear time series analysis method, which employs phase space reconstruction to investigate the recursive features of a dynamic system [41]. Generally, this method projects high-dimensional phase space to two dimensions, that is, the two-dimensional recurrence plot can reflect the trajectory of m dimensions. Our research group once employed this method to identify different two-phase flow patterns, and had good results [19]. Thus in this paper we utilise the recurrence plot method to analyse the voltage signals of gas–liquid two-phase flow. The result elucidates that the texture structure of the recurrence plot is pretty clear and obvious. The recurrence plot provides an effective method for gas–liquid two-phase flow pattern identification.

On the basis of Takens embedded theory [42], we can reconstruct a phase space from an original time series $x(i)$, $i=1, 2, \ldots, n$, as follows:

$$L(i)=[x(i),\ x(i+\tau),\ \ldots,\ x(i+(m-1)\tau)],\quad i=1,\ 2,\ \ldots,\ N \tag{11}$$

where m is embedded dimensions, τ is the time delay, and N is the number of phase space vectors. The representation of recurrence plots is given as follows:

$$R_{i,j}=\Theta(\varepsilon-||L(i)-L(j)||),\quad i,\ j=1,\ 2,\ \ldots,\ N \tag{12}$$

where $\Theta(\bullet)$ is the Heaviside function, ε is the threshold, and $||\bullet||$ is the Euclidean norm. When $\varepsilon-||L(i)-L(j)||>0$, $R_{i,j}=1$, and when $\varepsilon-||L(i)-L(j)||<0$, $R_{i,j}=0$; thus the matrix $R_{i,j}$ consists of the values of 0 or 1 only. The graphical representation for recurrence plots is $N\times N$ grid of points, which are presented as black for 1 and white for 0.

Texture features in the recurrence plots include scatter points, sections along with the diagonal direction, and sections along with the vertical direction or horizontal direction (they can work together to form rectangular blocks) [41]. The recurrence plot shows scatter points when the system status is isolated or not repetitive. When the trajectory in phase space is parallel to another one, or the trajectories in phase space at different times appear in the same area, the sections along with the diagonal direction are shown in the recurrence plot. When the system status remains unchanged in a period of time or changed very slowly, the corresponding recurrence plot shows black blocks which are formed by the sections in the vertical direction and horizontal direction, which indicates that there presents a periodic and repetitive status in the system.

We use the recurrence plot to analyse our experimental signals measured from the eight-electrode rotating field sensor. In the data processing, m, τ, and ε are set to 3, 4, and 0.25, respectively. The recurrence plots and the corresponding local magnified view of identical regions are shown in Figure 6. Specific results are depicted as follows:

Bubbly flow ($U_{sg}=0.147$ m/s, $U_{sw}=0.884$ m/s): In Figure 6a, the recurrence plot represents lots of scatter points, which can be explained by the stochastic motion of abundant minute gas bubbles leading to the most random characteristic.

Slug–bubble transitional flow ($U_{sg}=0.147$ m/s, $U_{sw}=0.442$ m/s): Based on the bubbly flow condition, the transitional flow occurs with the decrease of water superficial velocity. Scatter points still exist, which corresponds to the gas bubbles pasting through the sensor. At the same time, there are some gas slugs as well, which indicates the transition from bubbly flow to slug flow, as shown in Figure 6b.

Slug flow ($U_{sg}=0.147$ m/s, $U_{sw}=0.037$ m/s): As shown in Figure 6c, the alternating movement of gas slug and water slug leads to the quasi-periodicity of the voltage signal; thus there are many black blocks in the recurrence plot.

Furthermore, it is noteworthy that there exist a few gas bubbles between water slug and gas slug, due to which the recurrence plot still represents some scatter points.

Slug-churn transitional flow ($U_{sg}=0.295$ m/s, $U_{sw}=0.295$ m/s): When the gas superficial velocity is high, with the increase of the total superficial velocity, slug flow evolves into churn flow. During the flow transition, large gas slugs are broken into small ones and the interface between the water phase and gas phase becomes irregular, which can be reflected by the decrease of black blocks and the increase of lines along the diagonal in the recurrence plot in Figure 6d.

Churn flow ($U_{sg}=0.295$ m/s, $U_{sw}=0.589$ m/s): When the gas volume is big and the total flow velocities are high, the recurrence plot develops the texture along the diagonal, as shown in Figure 6e. There is some inner certainty in churn flow which leads to the texture lines.

4 A Scaling Exponent for Indicating the Inhomogeneous Distribution

On the basis of the signal data acquired by the conductance sensor measurement system, we select 20,000

measured points to carry out the multi-scale morphological analysis of the first-order difference sequence, and the maximum scale is set to 80. For the flow where the gas phase distribution is relatively uniform, the scatter points in the first-order difference scatter plot are located more closely to the coordinate origin. The second-order moment is small and it does not change obviously with the increase of scale. However, for the flow where the gas phase distribution is non-uniform, the scatter points in the plot distribute far away from the coordinate origin, which contributes to a relatively large second-order moment. Meanwhile, as the scale increases, the details of flow characteristics are ignored. Gas phase distribution is considered to be more uniform than that at lower scale. Hence, the scatter points gather towards the coordinate origin, and therefore, the second-order moment decreases obviously. When the scale increases to a certain value, the distribution and morphology of scatter points remain basically unchanged, that is, the second-order moment turns almost constant. Thus it is feasible to extract indexes for indicating the inhomogeneous distribution characteristics of the dispersed phase, that is, the gas phase in gas–liquid two-phase flow.

The evolutions of a multi-scale first-order difference plot constructed with three typical measurement signals from A-channel are shown in Figures 7–9, representing bubbly flow, slug–bubble transition flow, and slug flow, respectively. The scales are set to 1, 20, 50, and 80. The bisector of the second-fourth quadrant is regarded as the reference line to observe the evolution of scatter points along with the increase of scale on the first-third quadrant. It can be seen from the figures that there is the largest distribution range of scatter points for slug flow, less for slug–bubble transition flow, and the least for bubbly flow. At the same time, with increasing scale, the degree of scatter points approaching the coordinate origin is the biggest for slug flow, less for slug–bubble transition flow, and the least for bubbly flow. Specific analysis is given as follows.

The evolution of a multi-scale first-order difference plot of bubbly flow is presented in Figure 7. Combined with

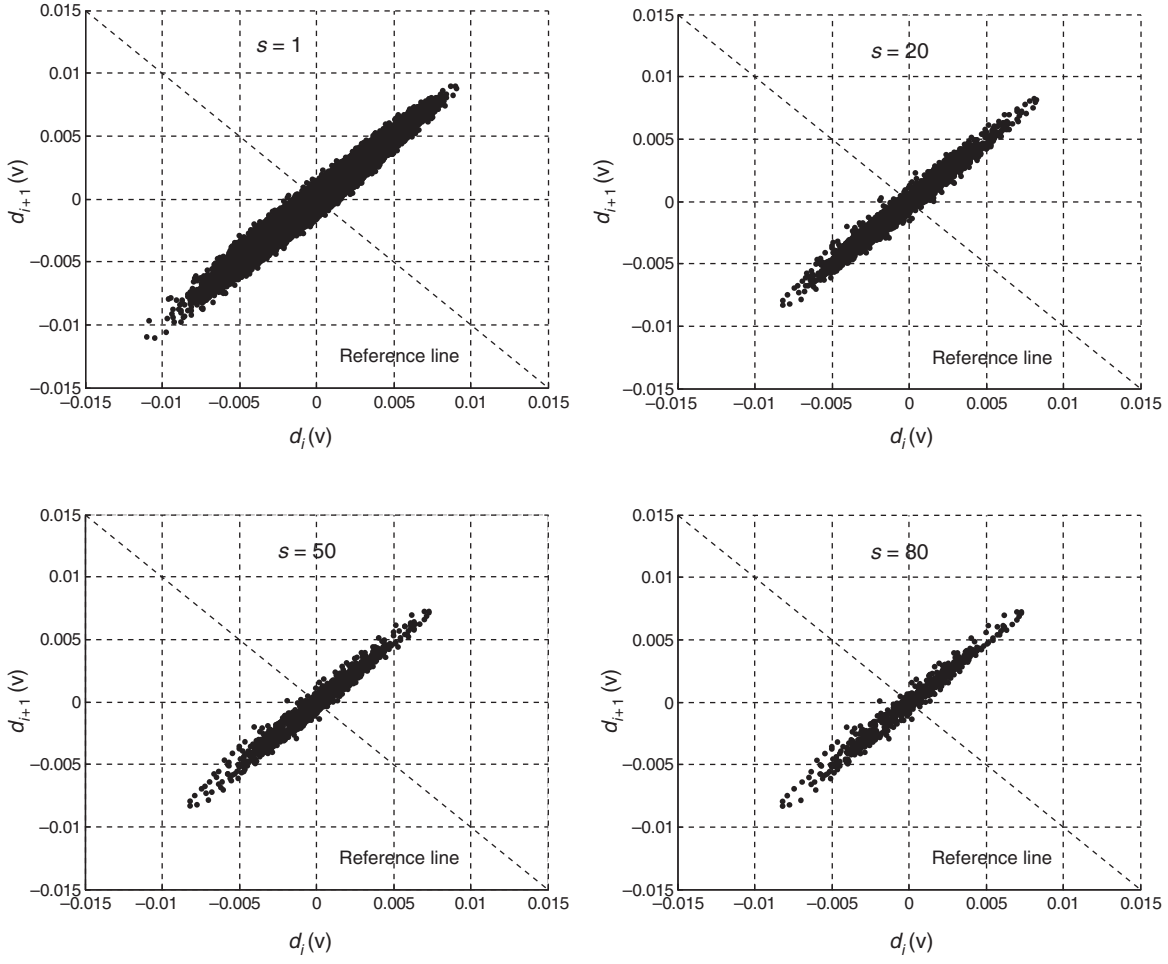

Figure 7: Multi-scale first-order difference scatter plot of bubbly flow ($U_{sg} = 0.147$ m/s, $U_{sw} = 0.884$ m/s).

the analysis in Section 3.3, we know that when the water superficial velocity is high enough, the gas phase exists in the form of bubbles, most of which are almost with the same size except several a little larger ones appearing occasionally. As a result, the first-order difference signal presents a continuous fluctuation with the amplitude maintaining a low value, and the corresponding scatter points concentrate near the coordinate origin. Therefore, the distribution area of scatter points in bubbly flow shrinks to the smallest one with the largest degree of the scatter points dispersing towards the second and fourth quadrants. In addition, the scatter points corresponding to the relatively large bubbles appearing occasionally are located far away from the coordinate origin. When the scale s is < 50, the distribution area reduces slightly as the scale increases. However, when the scale exceeds 50, with the increase of the scale, the scatter points exist in almost the same distribution range, which demonstrates the homogeneous distribution in the pipe under bubbly flow.

The result of the evolution of a multi-scale first-order difference scatter plot of slug–bubble transition flow is illustrated in Figure 8. The explicit behaviour of this flow is relatively short gas slugs flowing past with bubbles dispersed in long water slugs. As a result, the fluctuation of difference sequence exhibits a smaller frequency but larger amplitude. In terms of the corresponding first-order difference plot, for low scales, compared with the bubbly flow, the distribution of scatter points is almost identical with that of bubbly flow, except for its larger distribution area. In other words, the distribution area of scatter points shrinks in the second and fourth quadrants, but extends along with the bisector of the second-fourth quadrant, resulting in a stronger distribution trend than bubbly flow. Similarly, the corresponding scatter points of bubbles concentrate near the coordinate origin, but the corresponding scatter points of short gas slugs distribute away from the coordinate origin. Furthermore, it is noteworthy that the size discrepancies among short gas slugs and bubbles here are much larger than bubbly flow, that is, the degree of inhomogeneous distribution enhances. Thus, the distribution area of scatter points is larger. Meanwhile, with the increase of scale, the distribution area diminishes obviously.

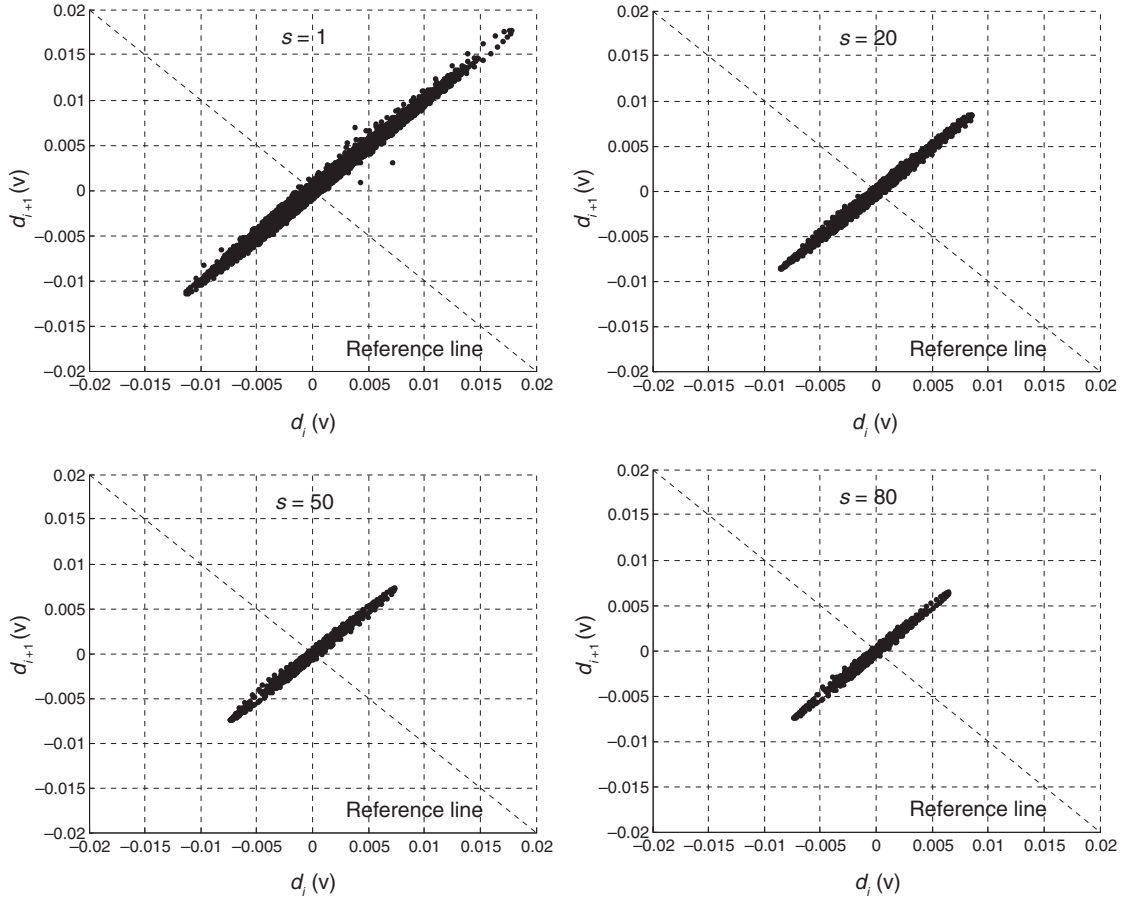

Figure 8: Multi-scale first-order difference scatter plot of slug–bubble transition flow ($U_{sg} = 0.147$ m/s, $U_{sw} = 0.442$ m/s).

The evolution of a multi-scale first-order difference plot of slug flow is shown in Figure 9. In slug flow, when there are no gas slugs flowing through the measuring area, the amplitude of the first-order difference sequence fluctuates slightly near zero; thus the corresponding scatter points concentrate near the coordinate origin. When gas slugs flow through the measuring area, the fluctuating range of difference sequence becomes severer; thus the distribution area extends along with the bisector of the first-third quadrant. Besides, with the increase of scale, the distribution area shrinks extremely obviously. That is because the gas distribution under slug flow is extremely non-uniform, where gas slugs and water slugs flow past alternately, resulting in the largest fluctuation range of difference sequence and the largest distribution area with the strongest distribution trend in the plot.

According to the characteristics of the foregoing distributions in the multi-scale first-order difference plot under three typical flow patterns, we extract two indexes, that is, the second-order moment $M_{1,2}(s)$ based on the bisector of the second-fourth quadrant as the reference line and the slope of $M_{1,2}(s)$ in all scales, to indicate the differences under different flow conditions and to investigate the inhomogeneous distribution characteristics of the gas phase in gas–liquid two-phase flow.

The curves of $M_{1,2}(s)$ with increasing scale and its fitted slope in all scales under five typical flow conditions obtained via fixing the gas superficial velocity and increasing the water superficial velocity are shown in Figures 10–12.

It can be concluded from Figure 10 that when fixing the gas superficial velocity at 0.055 m/s and then increasing the water superficial velocity gradually, long gas slugs are broken up into short ones, corresponding to the conversion process of almost all gas phase with little water flowing in the pipe to gas slugs and water slugs appearing alternately, resulting in more and more inhomogeneous distribution of the gas phase in the pipe and the larger slope value of the corresponding multi-scale second-order moment. In particular, the slope of the second-order moment reaches maximum at $U_{sw} = 0.147$ m/s, implying the most inhomogeneous distribution of the gas

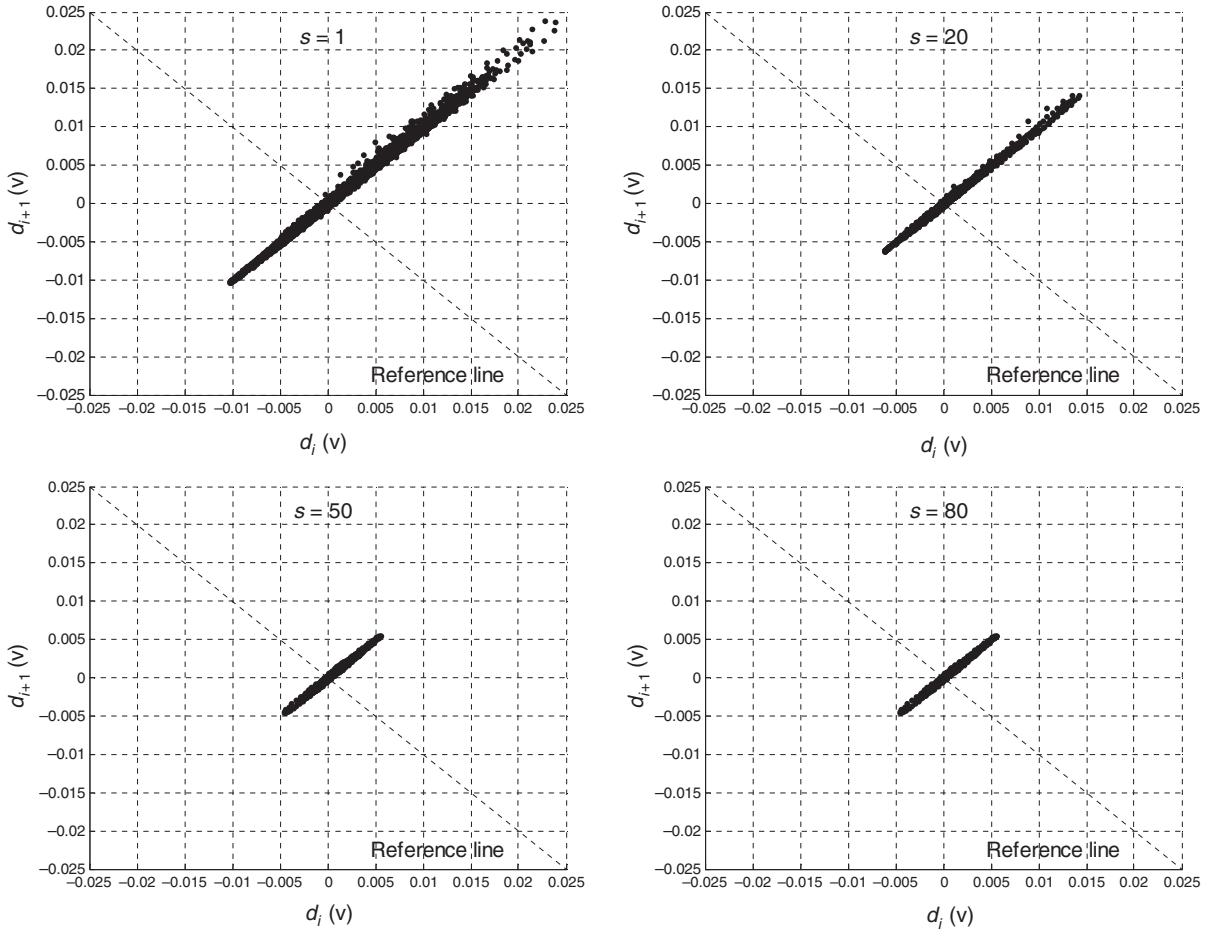

Figure 9: Multi-scale first-order difference scatter plot of slug flow ($U_{sg} = 0.147$ m/s, $U_{sw} = 0.037$ m/s).

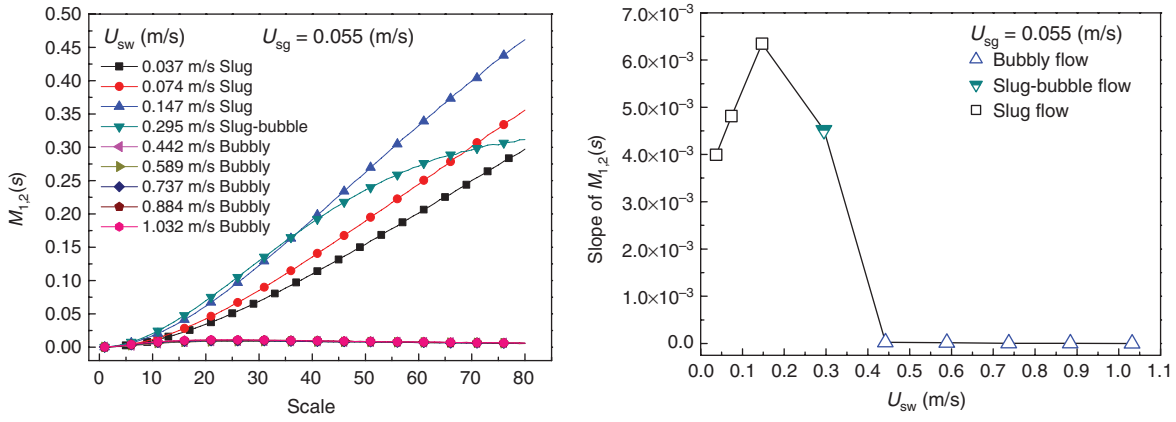

Figure 10: Multi-scale $M_{1,2}(s)$ and its fitted slope in the condition of increasing the water superficial velocity when fixing the gas superficial velocity at 0.055 m/s.

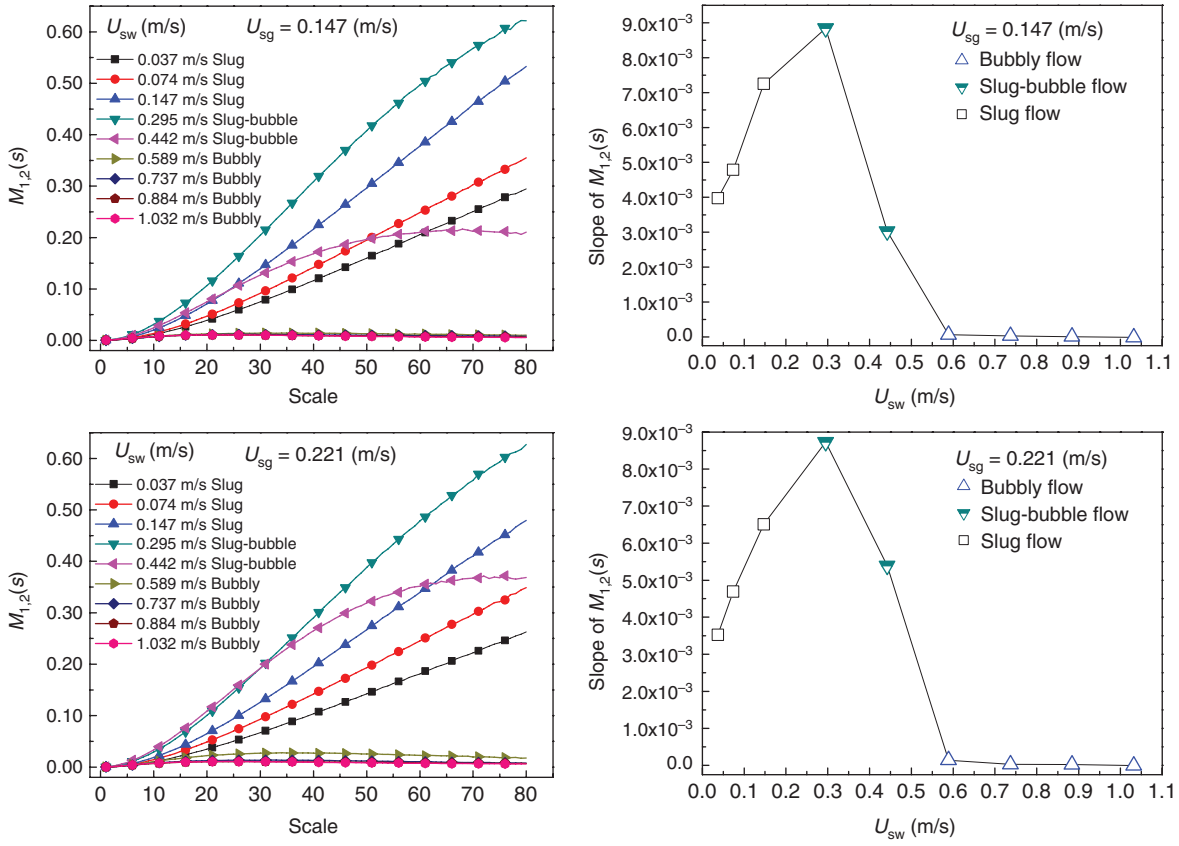

Figure 11: Multi-scale $M_{1,2}(s)$ and its fitted slope in the condition of increasing the water superficial velocity when fixing the gas superficial velocity at 0.147 and 0.221 m/s, respectively.

phase under this flow condition. Continuing to increase the water superficial velocity, as the turbulent energy becomes high enough to break several gas slugs up into bubbles, the degree of inhomogeneous distribution of the gas phase becomes lower and the slope decreases accordingly. With the water superficial velocity further increasing to 0.442 m/s, all gas slugs are broken up into bubbles of almost the same size. As a result, the degree of inhomogeneous distribution of the gas phase becomes the lowest and the slope reaches minimum.

Figure 11 exhibits the curves of $M_{1,2}(s)$ with increasing scale and its fitted slope when the gas superficial velocity is set to 0.147 m/s and 0.221 m/s, respectively. The variation trend of the curves is similar to that in Figure 10. However,

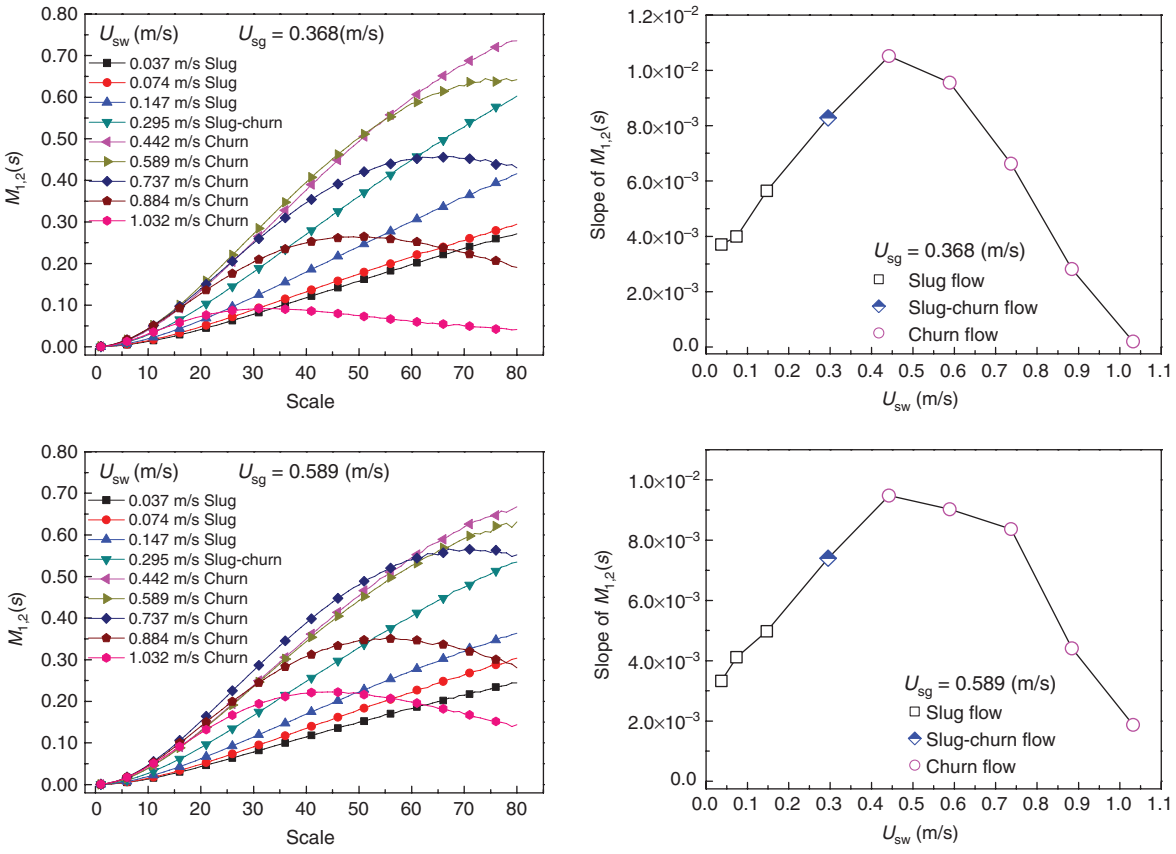

Figure 12: Multi-scale $M_{1,2}(s)$ and its fitted slope in the condition of increasing the water superficial velocity when fixing the gas superficial velocity at 0.368 and 0.589 m/s, respectively.

the gas superficial velocity is higher, which means the gas phase is more difficult to be broken up; thus the slope of $M_{1,2}(s)$ will reach the maximum at U_{sw} = 0.295 m/s instead of at U_{sw} = 0.147 m/s. As the water velocity continues to increase to 0.442 m/s, the gas slugs are shortened with more bubbles existing at the same time, and until the water superficial velocity is up to 0.589 m/s, the gas phase suspends in the water phase in the form of bubbles, which are almost with the uniform size. Therefore, the degree of inhomogeneous distribution of the gas phase presents the lowest and the slope of $M_{1,2}(s)$ becomes the smallest.

The curves of same criterions with the gas superficial velocity set to 0.368 and 0.589 m/s are shown in Figure 12. Similarly, the slope of $M_{1,2}(s)$ increases first and then decreases with the increase of water superficial velocity. But it is impossible for the gas phase to disintegrate into bubbles when the water superficial velocity is up to 0.147 m/s, and thus the flow pattern now is slug–churn transition flow instead of slug–bubble transition flow. Besides, it is difficult for the appearance of a very low slope, that is, the gas cannot be shattered into bubbles in the uniform size. As a result, the degree of inhomogeneous distribution of the gas phase is relatively high at all times.

In order to avoid overlapping of points with the same water superficial velocity and different gas superficial velocity, the relationship between the slope of $M_{1,2}(s)$ and gas superficial velocity as well as mixture velocity is provided in Figure 13, in which the horizontal axis represents the mixture velocity and the vertical axis represents the slope of $M_{1,2}(s)$. Additionally, the conditions with the same gas superficial velocity are presented with the same type of line, and different points with diverse shapes and colours symbolise different flow patterns. For the nine points in each line, the water superficial velocity is 0.037, 0.074, 0.147, 0.295, 0.442, 0.589, 0.737, 0.884, and 1.032 (m/s), respectively.

It can be seen from Figure 13 that when the gas superficial velocity is between 0.055 and 0.221 m/s, before the water superficial velocity increases to 0.147 m/s, corresponding to the process of long gas slugs shortened to be short ones, the flow pattern is the slug pattern and the degree of inhomogeneous distribution of the gas phase as well as the corresponding slope of $M_{1,2}(s)$ increases. When the water superficial velocity is up to 0.295 m/s, several gas slugs are broken up into bubbles, due to which the degree of inhomogeneous distribution of the gas phase continues to increase and the corresponding flow pattern is slug–bubble

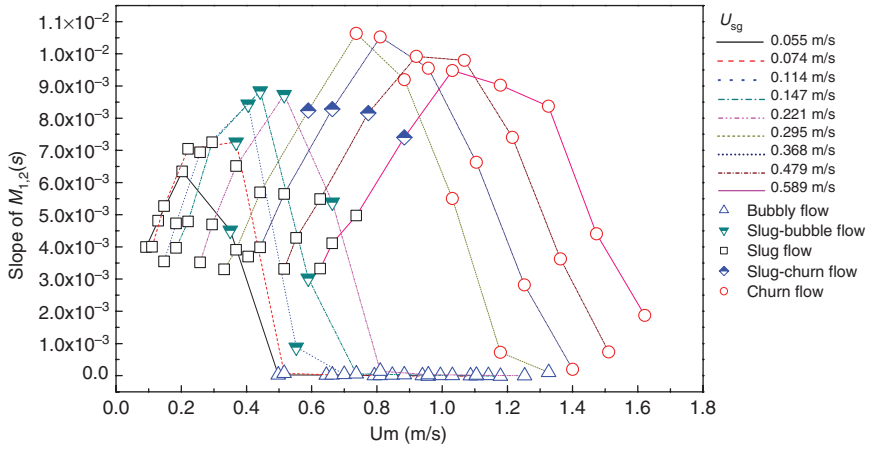

Figure 13: The slope of multi-scale $M_{1,2}(s)$ versus water cut and mixture velocity.

transition flow. Continuing to increase the water superficial velocity to 0.442 m/s, though the flow pattern is still slug–bubble transition flow, the gas slugs are so short that the degree of inhomogeneous distribution and the corresponding slope is lower. Until the water superficial velocity is up to 0.589 m/s, turbulent energy becomes high enough to break the gas slugs up into dispersed gas bubbles. Thereby, the degree of inhomogeneous distribution of the gas phase shows the lowest and the slope of $M_{1,2}(s)$ becomes the smallest. Notably, when the gas superficial velocity is relatively low, particularly at 0.055 and 0.074 m/s, slug–bubble transition flow appears only at $U_{sw}=0.295$ m/s, and the bubbly flow occurs at a lower velocity of water.

When the gas superficial velocity is between 0.295 and 0.589 m/s, the flow pattern of the first three points is slug flow as well and the slope of $M_{1,2}(s)$ increases. However, the turbulent energy breaks up the gas slugs into lots of churns with different sizes instead of bubbles when the water superficial velocity increases to 0.295 m/s. Thus the flow pattern is slug–churn transition flow, and the degree of inhomogeneous distribution of the gas phase increases as well and the slope becomes larger accordingly. With further increment of water superficial velocity, churn flow emerges and the degree of inhomogeneous distribution increases first, and then decreases as the gas churns tend to be with more uniform size, and the slope of $M_{1,2}(s)$ becomes smaller accordingly, but still larger than that under bubbly flow.

To shed light on the variation tendency of the slope of multi-scale second-order moment under different flow conditions, we summarise the analysis as follows: (1) The degree of inhomogeneous distribution of the gas phase increases first and then decreases with the increase of water superficial velocity. At lower gas superficial velocity, the gas phase exists in the form of bubbles when water velocity is high enough, leading to the most homogeneous distribution of the dispersed phase in the pipe. As a result, the slope of multi-scale second-order moment is much lower and remains almost constant. However, at higher gas superficial velocity, the gas phase exists in the form of churns when water velocity is high enough. Thus the degree of inhomogeneous distribution is higher and the slope is larger accordingly. (2) The slope of multi-scale second-order moment is different with different gas superficial velocities. At lower gas superficial velocity, due to the uniform structure of the gas phase, the slope is relatively low. On the contrary, when gas superficial velocity is higher, the slope is higher as well. It indicates that gas holdup has a strong influence on the distribution of the gas phase in gas–liquid two-phase flow. (3) The variation tendency of the slope at different gas superficial velocities is similar, which illuminates that the flow structure of the gas phase possesses a certain principle with the increase of water superficial velocity.

To better investigate the inhomogeneous distribution characteristics of the gas phase in gas–liquid two-phase flow, we further analyse the conduction fluctuating signals from the energy point of view based on the adaptive optimal kernel time–frequency representation (AOK TFR) [43]. The AOK TFRs of five typical flow patterns are shown in Figure 14.

For slug flow, the frequency mainly focuses on between 0 and 20 Hz with one or more peaks. The energy exhibits an intermittent feature in the time domain, which corresponds to the intermittent presence of long gas slugs. The frequency band of bubbly flow is quite wide. The energy distribution presents a dispersed characteristic in the time domain, which can be explained by the extremely dispersed bubble in the water phase. Meanwhile, the average energy of bubbly flow is relatively low. In churn flow, there exists obvious frequency peaks associated with the periodic oscillation. The energy distribution is

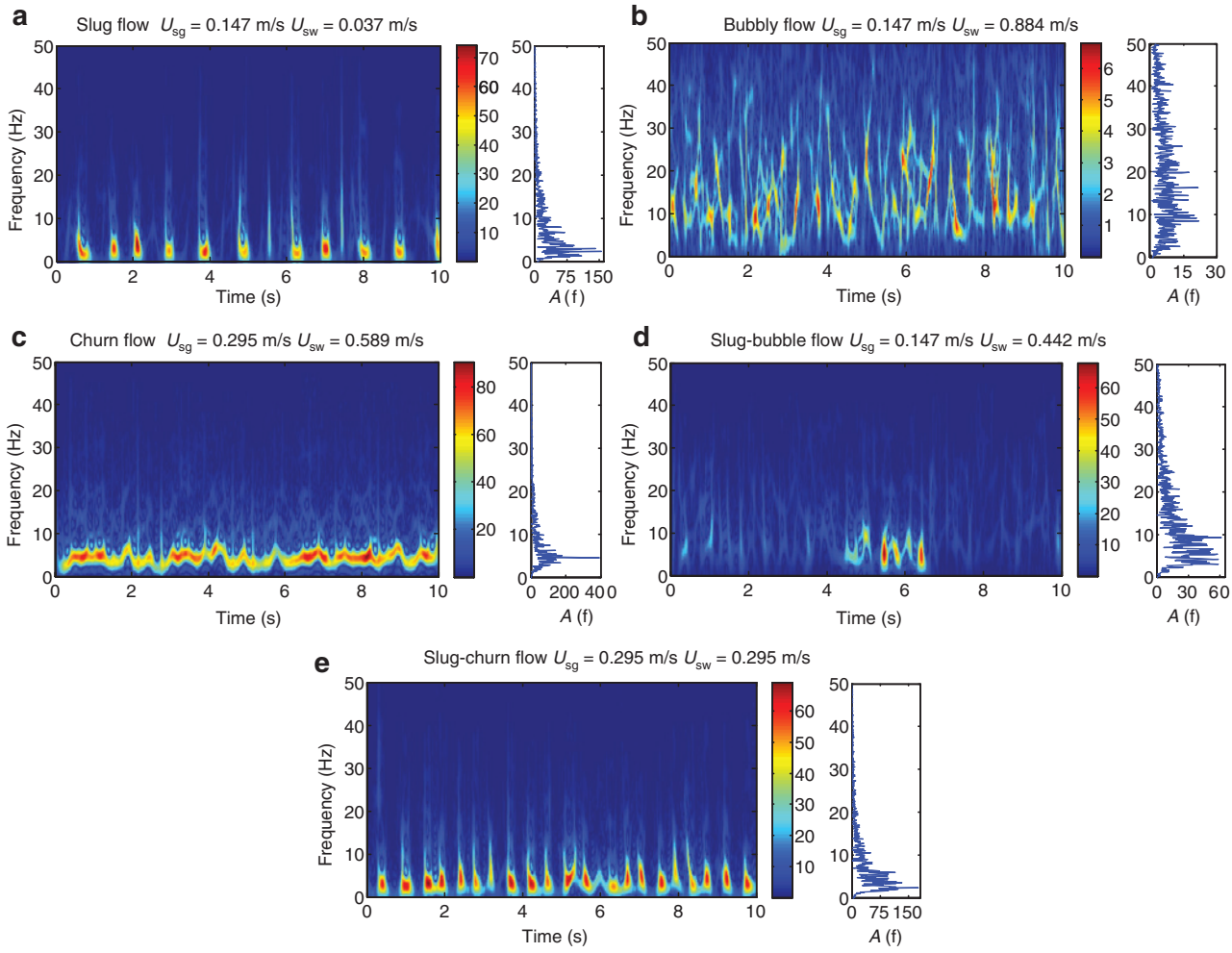

Figure 14: Time–frequency joint distribution of five typical flow patterns: (a) slug flow; (b) bubbly flow; (c) churn flow; (d) slug–bubble transitional flow; (e) slug–churn transitional flow.

continuous and uniform in the time domain, but have a high value, which corresponds to the flow behaviour that gas slugs pass through the sensor. In slug–bubble transitional flow, because of the movement of minute bubbles, there are no obvious peaks and a more wide frequency band than slug flow but the frequency band is not as wide as bubbly flow. In the AOK TFR plane, high energy and low energy appear alternatively, which can be explained by the behaviour that gas slugs and gas bubbles pass through the sensor alternatively. The frequency of slug–churn transitional flow mainly gathered around 0–20 Hz; however, there is a peak between 0 and 5 Hz. Besides, the frequency distribution is rare before the peak; normally there is a mutation when the signal comes to peak. The energy distribution presents a continuous feature but with occasional low energy. This explains the fact that the flow pattern is not stable in both churn flow and slug flow.

On the basis of the AOK TFR plane, we calculate the total energy E, whose value is low when the flow is stable, and vice versa. Correspondingly in Figure 15, the outcomes reveal that the increasing U_{sw} enhances the total energy in the AOK TFR plane first. The slug flow structure with higher energy leads to more violent signal fluctuations and more inhomogeneous distribution of the gas phase in water phase flow. Slug–bubble transitional flow occurs as the water superficial velocity increases when fixing the gas superficial velocity between 0.055 and 0.221 m/s. The energy increases first because the tremendous turbulent kinetic energy breaks long gas slugs up to short ones and blisters and the system is more unstable. This explains that the degree of inhomogeneous distribution of the gas phase increases at this moment. When the water superficial velocity continues to increase, the energy decreases, which illustrates that the flow tends to be more stable. There are few gas slugs and more gas bubbles. Though the flow pattern is still slug–bubble transitional flow, the degree of inhomogeneous distribution of the gas phase becomes lower relatively. For the gas superficial velocity

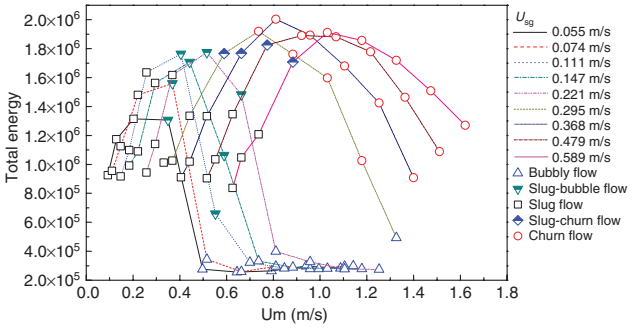

Figure 15: The total energy E versus water cut and mixture velocity.

between 0.295 and 0.589 m/s, the slug flow evolves to slug–churn transitional flow with the increase of water superficial velocity. The total energy is higher than before, which can be explained by the fact that at this moment the gas phase exists in the form of gas slugs and blocks, which corresponds to a more unstable flow structure, leading to higher energy and a more inhomogeneous distribution of the gas phase. For churn flow, the increasing water superficial velocity leads to breakup of gas blocks, resulting in uniform gas block sizes. Thus the flow becomes more and more stable, the energy and the degree of inhomogeneous distribution of the gas phase decrease gradually as well. In bubbly flow, numbers of gas bubbles with the uniform size are distributed randomly in the pipe. In this case, the system is so stable that the energy is the lowest and the degree of inhomogeneous distribution of the gas phase reaches the lowest value.

From Figures 13 and 15, we find that the trends of the slope of $M_{1,2}(s)$ and the total energy in the AOK TFR plane are accordant during the evolvement of gas–liquid two-phase flow structure. Besides, the energy is a dynamic factor indicating the system stability and the process of breakup and coalescence of the gas phase. Thus it can be seen that the multi-scale morphological analysis method based on the first-order difference scatter plot can effectively depict the system stability of two-phase flow and can indicate the inhomogeneous distribution of the gas phase in gas–liquid two-phase flow.

5 Conclusions

The flow structures encountered in gas–liquid two-phase flow are of extremely complex nature, especially for the gas phase which performs a compound inhomogeneous distribution. The measuring signal of a conductance sensor is capable of reflecting the different sizes of the gas phase and its distribution. Its first-order difference sequence therefore can indicate the size variation of the dispersed gas phase more distinctly. Hence, this paper extracts a scale exponent, that is, second-order moment from the first-order difference plot based on the conductance sensor signals measured from gas–liquid two-phase flow, and we conclude that the invariant exponent is sensitive to the inhomogeneous distribution of the dispersed gas phase. In addition, we further explore the dynamic mechanism of gas–liquid two-phase flow by using the

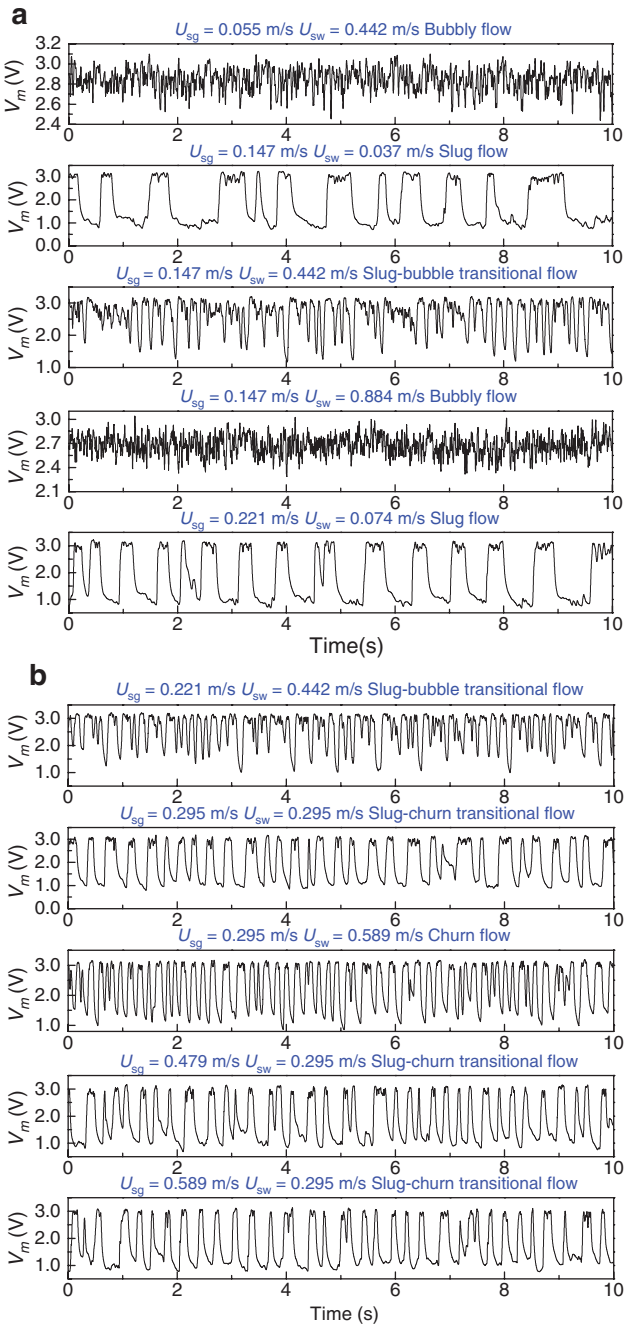

Figure 16: The measurement voltage from A-channel.

AOK TFR from the viewpoint of energy. The conclusions are stated as follows:

1. Fixing gas superficial velocity, the degree of inhomogeneous distribution of the dispersed phase under slug flow enhances with the increase of water superficial velocity. This result is due to the fact that the gas phase exists in the form of large slugs at low water velocity, and as the water velocity increases, some gas slugs are broken up into short ones, exhibiting gas slugs and water slugs appearing alternately.
2. For churn flow, when fixing gas superficial velocity and increasing water superficial velocity gradually, the size of gas churns in churn flow tend to be more and more uniform, due to which the degree of inhomogeneous distribution of the dispersed phase decreases.
3. In bubbly flow, the water superficial velocity is so high that the gas phase is broken up into bubbles in the uniform size. As a result, the degree of inhomogeneous distribution of the dispersed phase is much

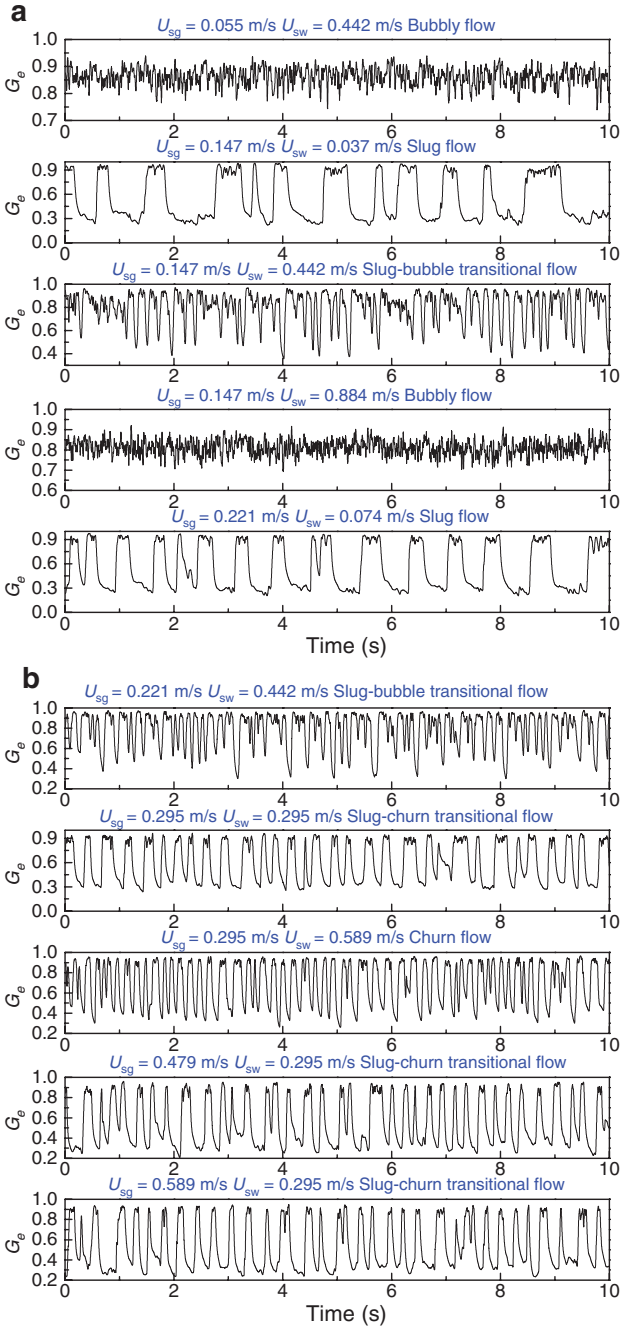

Figure 17: Normalised conductance sequences.

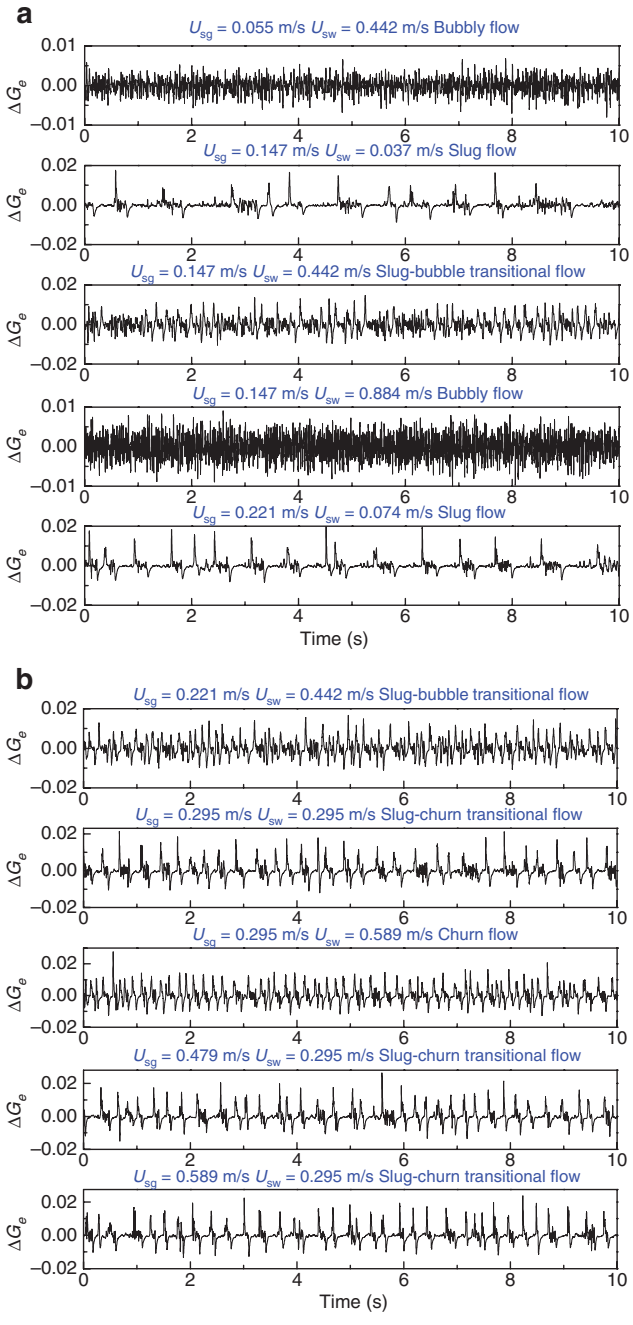

Figure 18: First-order difference sequences.

Table 1: The second-order moments of five flow conditions.

Scale factor s	$U_{sg}=0.055$ $U_{sw}=0.442$	$U_{sg}=0.147$ $U_{sw}=0.037$	$U_{sg}=0.147$ $U_{sw}=0.442$	$U_{sg}=0.147$ $U_{sw}=0.884$	$U_{sg}=0.221$ $U_{sw}=0.074$
1	0.000079	0.000125	0.000285	0.000157	0.000159
2	0.000311	0.000497	0.001132	0.000604	0.000635
3	0.000678	0.001110	0.002522	0.001282	0.001419
4	0.001160	0.001958	0.004424	0.002119	0.002499
5	0.001730	0.003029	0.006802	0.003042	0.003863
6	0.002360	0.004314	0.009619	0.003987	0.005495
7	0.003020	0.005802	0.012832	0.004903	0.007381
8	0.003700	0.007481	0.016402	0.005758	0.009503
9	0.004360	0.009340	0.020291	0.006536	0.011849
10	0.005010	0.011368	0.024461	0.007228	0.014402
11	0.005610	0.013553	0.028879	0.007833	0.017147
12	0.006180	0.015889	0.033510	0.008341	0.020077
13	0.006700	0.018360	0.038328	0.008782	0.023167
14	0.007160	0.020968	0.043294	0.009126	0.026423
15	0.007580	0.023697	0.048395	0.009438	0.029818
16	0.007950	0.026530	0.053604	0.009667	0.033361
17	0.008270	0.029480	0.058881	0.009843	0.037027
18	0.008540	0.032523	0.064228	0.009958	0.040789
19	0.008780	0.035659	0.069632	0.010086	0.044667
20	0.008970	0.038886	0.075016	0.010122	0.048668
21	0.009130	0.042189	0.080430	0.010075	0.052738
22	0.009280	0.045581	0.085770	0.010130	0.056910
23	0.009380	0.049052	0.091180	0.010126	0.061234
24	0.009480	0.052590	0.096546	0.010192	0.065523
25	0.009470	0.056201	0.101747	0.010110	0.069945
26	0.009530	0.059832	0.106894	0.010122	0.074415
27	0.009570	0.063578	0.112119	0.010062	0.078873
28	0.009590	0.067401	0.117147	0.009982	0.083538
29	0.009610	0.071165	0.121946	0.009903	0.088203
30	0.009640	0.075050	0.126929	0.009827	0.092869
31	0.009490	0.078986	0.131538	0.009791	0.097500
32	0.009560	0.083016	0.136109	0.009637	0.102403
33	0.009510	0.086861	0.140719	0.009647	0.107088
34	0.009330	0.091041	0.145146	0.009568	0.112187
35	0.009330	0.094987	0.149425	0.009627	0.116867
36	0.009280	0.099264	0.153390	0.009332	0.121582
37	0.009250	0.103443	0.157425	0.009387	0.126910
38	0.009170	0.107581	0.161289	0.009233	0.131705
39	0.009130	0.111891	0.164635	0.009125	0.136970
40	0.009010	0.116123	0.168737	0.009017	0.141962
41	0.009040	0.120484	0.171952	0.009171	0.146875
42	0.008900	0.124651	0.175180	0.008970	0.151977
43	0.008870	0.128949	0.178769	0.009033	0.157296
44	0.008650	0.133479	0.181200	0.008802	0.162349
45	0.008610	0.137839	0.183793	0.008889	0.167732
46	0.008430	0.142096	0.186382	0.008610	0.172592
47	0.008530	0.146757	0.189367	0.008329	0.177689
48	0.008260	0.151017	0.192468	0.008451	0.182918
49	0.008260	0.155576	0.193945	0.008489	0.188119
50	0.008140	0.159885	0.196665	0.008326	0.193320
51	0.008150	0.164761	0.198175	0.008215	0.198237
52	0.008120	0.169377	0.199836	0.008222	0.202976
53	0.008070	0.173782	0.202098	0.008187	0.208610
54	0.007890	0.177137	0.202661	0.007971	0.214901
55	0.007810	0.182264	0.204764	0.008187	0.218977
56	0.007670	0.187870	0.206448	0.007674	0.224426
57	0.007530	0.191257	0.207655	0.007793	0.229815
58	0.007490	0.196328	0.207922	0.007628	0.234235

Table 1 (continued)

Scale factor s	U_{sg}=0.055 U_{sw}=0.442	U_{sg}=0.147 U_{sw}=0.037	U_{sg}=0.147 U_{sw}=0.442	U_{sg}=0.147 U_{sw}=0.884	U_{sg}=0.221 U_{sw}=0.074
59	0.007450	0.200917	0.209085	0.007567	0.240331
60	0.007160	0.205538	0.209955	0.007665	0.245520
61	0.007160	0.209729	0.212178	0.007526	0.251149
62	0.007230	0.214541	0.211531	0.007441	0.255268
63	0.007030	0.219292	0.212553	0.007278	0.261330
64	0.007080	0.223117	0.213173	0.007333	0.265583
65	0.006810	0.227430	0.214873	0.007294	0.271700
66	0.006770	0.232750	0.213015	0.007185	0.277515
67	0.006850	0.236679	0.213086	0.007061	0.281182
68	0.006550	0.241118	0.216324	0.007048	0.286814
69	0.006550	0.246605	0.214197	0.006987	0.291426
70	0.006270	0.250400	0.211922	0.007036	0.297090
71	0.006360	0.255364	0.213355	0.007082	0.302428
72	0.006250	0.259652	0.211925	0.006637	0.307324
73	0.006200	0.263699	0.211624	0.006437	0.313608
74	0.006380	0.267455	0.210851	0.006506	0.319613
75	0.005940	0.273286	0.210565	0.006689	0.321808
76	0.006200	0.278283	0.211467	0.006560	0.324923
77	0.005910	0.283395	0.208147	0.006500	0.334979
78	0.005830	0.285457	0.209712	0.006369	0.337549
79	0.005880	0.290118	0.205988	0.006508	0.344321
80	0.005730	0.294768	0.210333	0.006420	0.348786

The unit of U_{sg} and U_{sw} is m/s.

Table 2: The second-order moments of five flow conditions.

Scale factor s	U_{sg}=0.221 U_{sw}=0.442	U_{sg}=0.295 U_{sw}=0.295	U_{sg}=0.295 U_{sw}=0.589	U_{sg}=0.479 U_{sw}=0.295	U_{sg}=0.589 U_{sw}=0.295
1	0.000377	0.000329	0.000491	0.000348	0.000314
2	0.001500	0.001309	0.001953	0.001383	0.001240
3	0.003350	0.002918	0.004359	0.003080	0.002770
4	0.005895	0.005126	0.007669	0.005405	0.004850
5	0.009100	0.007901	0.011839	0.008324	0.007450
6	0.012924	0.011207	0.016822	0.011797	0.010530
7	0.017325	0.015010	0.022570	0.015791	0.014070
8	0.022258	0.019276	0.029038	0.020267	0.018020
9	0.027681	0.023977	0.036178	0.025198	0.022360
10	0.033551	0.029075	0.043946	0.030543	0.027050
11	0.039827	0.034554	0.052295	0.036278	0.032070
12	0.046478	0.040377	0.061180	0.042377	0.037410
13	0.053453	0.046532	0.070567	0.048815	0.043030
14	0.060724	0.052980	0.080386	0.055543	0.048910
15	0.068245	0.059722	0.090661	0.062574	0.055050
16	0.075990	0.066715	0.101284	0.069841	0.061430
17	0.083944	0.073950	0.112195	0.077376	0.068000
18	0.092051	0.081419	0.123425	0.085149	0.074760
19	0.100264	0.089049	0.134902	0.093072	0.081680
20	0.108600	0.096883	0.146666	0.101242	0.088750
21	0.117014	0.104927	0.158466	0.109419	0.096060
22	0.125433	0.113093	0.170672	0.117800	0.103410
23	0.133904	0.121408	0.182836	0.126372	0.110940
24	0.142435	0.129919	0.195010	0.135164	0.118610
25	0.150915	0.138385	0.207458	0.143877	0.126300

Table 2 (continued)

Scale factor s	$U_{sg}=0.221$ $U_{sw}=0.442$	$U_{sg}=0.295$ $U_{sw}=0.295$	$U_{sg}=0.295$ $U_{sw}=0.589$	$U_{sg}=0.479$ $U_{sw}=0.295$	$U_{sg}=0.589$ $U_{sw}=0.295$
26	0.159261	0.147155	0.219925	0.152831	0.134180
27	0.167684	0.155841	0.232446	0.161721	0.142010
28	0.175902	0.164591	0.244892	0.170769	0.150060
29	0.183939	0.173606	0.257564	0.179840	0.158080
30	0.191920	0.182439	0.270015	0.188804	0.166030
31	0.199922	0.191515	0.282317	0.198049	0.174430
32	0.207710	0.200698	0.294850	0.207425	0.182540
33	0.215448	0.209476	0.306852	0.216166	0.190480
34	0.223295	0.218847	0.319455	0.225393	0.198650
35	0.230408	0.227779	0.331240	0.234465	0.207120
36	0.237877	0.237060	0.343461	0.243979	0.215320
37	0.244511	0.246172	0.354893	0.253169	0.223740
38	0.251162	0.255615	0.366918	0.262538	0.231870
39	0.258270	0.264733	0.378946	0.271379	0.240060
40	0.264845	0.273713	0.390065	0.280738	0.248410
41	0.270533	0.283290	0.401011	0.290217	0.256260
42	0.277157	0.291524	0.411997	0.298940	0.264810
43	0.282360	0.300786	0.422742	0.307972	0.272850
44	0.288787	0.309709	0.433147	0.316773	0.280520
45	0.294037	0.318325	0.444202	0.326746	0.288820
46	0.299044	0.327429	0.453229	0.335138	0.297260
47	0.304866	0.336529	0.464340	0.343417	0.304970
48	0.310051	0.346755	0.473160	0.352664	0.312360
49	0.313939	0.353916	0.483999	0.360502	0.320900
50	0.319044	0.363740	0.492530	0.369515	0.329070
51	0.322434	0.370886	0.500528	0.379126	0.336580
52	0.326812	0.380579	0.509874	0.386884	0.344270
53	0.331693	0.389571	0.518972	0.395569	0.353730
54	0.333811	0.397057	0.526559	0.403823	0.360480
55	0.337805	0.405696	0.531931	0.412835	0.367410
56	0.339836	0.416067	0.539848	0.421157	0.375210
57	0.343752	0.422929	0.545674	0.426214	0.383630
58	0.348586	0.432030	0.552393	0.437870	0.390800
59	0.350455	0.440528	0.559368	0.445349	0.397080
60	0.351413	0.448851	0.567597	0.452817	0.404910
61	0.355565	0.457653	0.572541	0.460414	0.412390
62	0.357410	0.465348	0.577971	0.466426	0.420480
63	0.356273	0.473155	0.582816	0.477138	0.428590
64	0.360935	0.481941	0.588618	0.481535	0.434430
65	0.359345	0.489929	0.594539	0.490609	0.442290
66	0.363238	0.496726	0.595926	0.498555	0.448020
67	0.363159	0.505252	0.596500	0.505707	0.454400
68	0.365658	0.511799	0.604741	0.510777	0.464530
69	0.366493	0.521103	0.605295	0.518539	0.468250
70	0.367150	0.528204	0.604554	0.526847	0.474040
71	0.367760	0.537666	0.610182	0.535538	0.479890
72	0.371293	0.543083	0.614693	0.538893	0.488880
73	0.366345	0.549998	0.621255	0.545326	0.495780
74	0.369341	0.557256	0.614518	0.551569	0.500070
75	0.368005	0.562754	0.616552	0.557693	0.506060
76	0.371587	0.573198	0.616106	0.563656	0.513260
77	0.366852	0.576808	0.619369	0.569233	0.522470
78	0.365213	0.583455	0.621976	0.574897	0.525570
79	0.366835	0.590780	0.618143	0.580162	0.532090
80	0.368298	0.599208	0.612001	0.589271	0.534600

The unit of U_{sg} and U_{sw} is m/s.

lower than that in slug flow or churn flow. In addition, the degree of inhomogeneous distribution of the dispersed phase does not change obviously with different water or gas superficial velocities.

4. The total energy calculated based on the AOK TFR plane acts as an intrinsic factor influencing the degree of inhomogeneous distribution of the dispersed phase in gas–liquid two-phase flow.

Acknowledgments: This study was supported by the National Natural Science Foundation of China (Grant Nos. 51527805, 11572220) and Tianjin City High School Science and Technology Fund Planning Project (Grant No. 20130718).

Appendix A: Raw Data

According to the experimental procedure introduced in Section 3, we obtain the measurement voltage and show 10 samples for example, which are delineated in Figure 16.

Appendix B: Normalised Conductance Sequences

According to (9), $G_e = V_m / V_m^w$, where V_m is the mixture measurement voltage and V_m^w is the mean pure water measurement voltage for the corresponding channel. Therefore, V_m corresponds to the data in Appendix A, and $V_m^w = 3.3$ V. Finally, we can obtain the normalised conductance sequences shown in Figure 17.

Appendix C: First-Order Difference Sequences

According to (10), we can obtain the first-order difference sequences based on the normalised conductance sequences shown in Figure 18.

Appendix D: Moments

First we plot the scatter points after the first return of the first-order difference sequence in the two-dimensional plane. Then we calculate the second-order moment $M_{1,2}(s)$ with the bisector of the second-fourth quadrant being the reference line. The moments with different scale factors s from 1 to 80 are presented in Tables 1 and 2.

Nomenclature

A	maximum value of input voltage (V)
$d_i(k)$	distance between the kth scatter point and the reference line (dimensionless)
d_i^s	difference sequence (dimensionless)
G_e	normalised conductance (dimensionless)
ΔG_e	first-order difference sequences of normalised conductance (dimensionless)
i, j, k	point index (dimensionless)
n	length of the sequence (dimensionless)
m	embedded dimension (dimensionless)
M	total number of scatter points (dimensionless)
$M_{i,j}(s)$	attractor moment in scale s (dimensionless)
s	scale factor (dimensionless)
u_c	combined standard uncertainty (dimensionless)
U_{sg}	gas superficial velocity (m/s)
U_{sw}	liquid superficial velocity (m/s)
V_m	mean mixture measurement voltage (V)
V_m^w	mean pure water measurement voltage (V)
x_i	ith coordinate component of the scatter point (dimensionless)
$x(i)$	one-dimensional time series (dimensionless)
$X(k)$	coordinate of the kth scatter point in the two-dimensional plane (dimensionless)
y_j^s	coarse-grained time series for $x(i)$ in scale s (dimensionless)
$\Theta(\bullet)$	Heaviside function
$\|\bullet\|$	Euclidean norm

Greek letter

α_i	orthogonal vector corresponding to the ith reference section (dimensionless)
ω	electric angle of input voltage (rad/s)
δ_m	gas–liquid mixture conductance (S)
δ_w	pure water conductance (S)
τ	time delay (dimensionless)
ε	threshold value of distance (dimensionless)

References

[1] G. F. Hewitt, Measurement of Two-Phase Flow Parameters, Academic Press, London 1978.
[2] G. Hetsroni, Handbook of Multiphase Systems, Hemisphere, New York 1982.
[3] C. T. Crowe, Multiphase Flow Handbook, CRC Press, New York 2006.
[4] G. B. Wallis, One-Dimensional Two-Phase Flow, McGraw-Hill Book Company, New York 1969.

[5] D. Barnea, O. Shoham, and Y. Taitel, Int. J. Multiphase Flow **6**, 387 (1980).
[6] M. G. Hubbard and A. E. Dukler, Proc. Heat Transfer Fluid Mech. Inst. **1**, 100 (1966).
[7] O. C. Jones, Jr. and N. Zuber, Int. J. Multiphase Flow **2**, 273 (1975).
[8] M. A. Vince and R. T. Lahey, Int. J. Multiphase Flow **8**, 93 (1982).
[9] G. Matsui, Int. J. Multiphase Flow **10**, 711 (1984).
[10] L. Y. Lao, Z. C. Zheng, Y. X. Wu, and D. H. Li, Adv. Mech. **32**, 235 (2002) (in Chinese).
[11] S. H. Lee, S. D. Kim, and S. H. Park, Korean J. Chem. Eng. **19**, 1020 (2002).
[12] B. R. Bakshi, H. Zhong, P. Jiang, and L. S. Fan, Chem. Eng. Res. Des. **75**, 608 (1995).
[13] T. Elperin and M. Klochko, Exp. Fluids **32**, 674 (2002).
[14] V. T. Nguyen, D. J. Euh, and C. H. Song, Int. J. Multiphase Flow **36**, 755 (2010).
[15] N. E. Huang, Z. Shen, S. R. Long, M. C. Wu, H. H. Shih, Q. Zheng, N. C. Yen, C. C. Tung, and H. H. Liu, Proc. R. Soc. London Ser. A **454**, 903 (1998).
[16] E. P. Wigner, Phys. Rev. **40**, 749 (1932).
[17] J. Ville, Cables Transmission **2**, 61(1948).
[18] Z. He, D. Zhang, B. Cheng, and W. Zhang, AIChE J. **43**, 345 (1997).
[19] M. Du, N. D. Jin, Z. K. Gao, and B. Sun, Chem. Eng. Sci. **82**, 144 (2012).
[20] G. Górski, G. Litak, R. Mosdorf, and A. Rysak, Zeitschrift Fur Naturforschung A **70**, 843 (2015).
[21] Z. K. Gao, L. D. Hu, and N. D. Jin, Chin. Phys. B **5**, 226 (2013).
[22] Y. Taitel, D. Barnea, and A. E. Dukler, AIChE J. **26**, 345 (1980).
[23] J. Weisman and S. Y. Kang, Int. J. Multiphase Flow **7**, 271 (1981).
[24] N. Brauner, Int. J. Multiphase Flow **27**, 885 (2001).
[25] J. M. Hay, C. Hudson, and C. L. Briens, Chem. Eng. J. **64**, 157 (1996).
[26] H. W. Li, Y. L. Zhou, B. Sun, and Y. Yang, Chin. J. Chem. Eng. **18**, 880 (2010).
[27] C. Tan, J. Zhao, and F. Dong, ISA Trans. **55**, 241 (2015).
[28] M. E. Cohen, D. L. Hudson, and P. C. Deedwania, IEEE Eng. Med. Biol. Mag. **15**, 97 (1996).
[29] P. Maurer, H. D. Wang, and A. Babloyantz, Phys. Rev. E **56**, 1188 (1997).
[30] J. Jeong, J. C. Gore, and B. S. Peterson, IEEE Trans. Biomed. Eng. **49**, 1374 (2002).
[31] J. Jeong, J. C. Gore, and B. S. Peterson, Biol. Cybern. **86**, 335 (2002).
[32] R. A. Thuraisingham, Cardiol. Res. Pract. **2009**, 807379 (2010).
[33] C. Y. Huo, J. J. Zhuang, X. L. Huang, F. Z. Hou, and X. B. Ning, Acta Physica Sinica **19**, 62 (2012) (in Chinese).
[34] C. Y. Huo, X. L. Huang, J. J. Zhuang, F. Z. Hou, H. J. Ni, et al., Physica A **392**, 3601 (2013).
[35] M. Annunziato and H. D. I. Abarbanel, Proceedings of International Conference on Soft Computing, SOCO, Genova, Italy 1999.
[36] F. X. Llauro and M. F. Llop, Int. J. Multiphase Flow **32**, 1397 (2006).
[37] N. Xiao and N. D. Jin, Acta Physica Sinica **56**, 5149 (2007) (in Chinese).
[38] Z. Y. Wang, N. D. Jin, Z. K. Gao, Y. B. Zong, and T. Wang, Chem. Eng. Sci. **65**, 5226 (2010).
[39] Z. Q. Wang, Y. F. Han, Y. Y. Ren, A. Zhao, and N. D. Jin, Chem. Eng. Sci. **141**, 104 (2016).
[40] M. Costa, A. L. Goldberger, and C. K. Peng, Phys. Rev. Lett. **89**, 068102 (2002).
[41] J. P. Eckmann and D. Ruelle, Europhys. Lett. **4**, 973 (1987).
[42] F. Takens, Lect. Notes Math **898**, 366 (1981).
[43] D. L. Jones and R. C. Baraniuk, IEEE Trans. Signal Process **43**, 2361 (1995).